Journal of Applied Physics

TUTORIAL | NOVEMBER 04 2022

Slit-scanning Raman microscopy: Instrumentation and applications for molecular imaging of cell and tissue

Yasuaki Kumamoto ; Menglu Li ; Kota Koike ; Katsumasa Fujita

J. Appl. Phys. 132, 171101 (2022)
https://doi.org/10.1063/5.0102079

AIP Publishing

Journal of Applied Physics TUTORIAL scitation.org/journal/jap

Slit-scanning Raman microscopy: Instrumentation and applications for molecular imaging of cell and tissue

Cite as: J. Appl. Phys. **132**, 171101 (2022); doi: 10.1063/5.0102079
Submitted: 6 June 2022 · Accepted: 10 October 2022 ·
Published Online: 4 November 2022

Yasuaki Kumamoto,[1,2,a)] Menglu Li,[1,3] Kota Koike,[1,3,b)] and Katsumasa Fujita[1,2,3]

AFFILIATIONS

[1]Department of Applied Physics, Osaka University, Suita, Osaka 565-0871, Japan
[2]Institute for Open and Transdisciplinary Research Initiatives, Osaka University, Suita, Osaka 565-0871, Japan
[3]AIST-Osaka University Advanced Photonics and Biosensing Open Innovation Laboratory, National Institute of Advanced Industrial Science and Technology (AIST), Suita, Osaka 565-0871, Japan

[a)]**Author to whom correspondence should be addressed:** kumamoto@ap.eng.osaka-u.ac.jp
[b)]Currently at OXIDE Corporation.

ABSTRACT

In recent years, Raman microscopy has emerged as a molecular imaging tool for cell and tissue analysis. A key reason for this is the development of techniques that significantly increase imaging speed. In this Tutorial, we introduce slit-scanning Raman microscopy, a Raman imaging technique that achieves imaging speeds more than two orders of magnitude faster than conventional confocal Raman microscopy, and its application to cell and tissue imaging and analysis. Recent advances in Raman imaging, particularly further improvements in imaging speed, sensitivity, specificity, and spatial resolution, are also discussed. In addition, we present the prospects of Raman microscopy as a molecular imaging method to aid in new discoveries in life sciences and the potential of high-speed Raman imaging for clinical applications.

I. INTRODUCTION

Fluorescence microscopy is an essential modality for visualizing the structures and functions of living organisms by biomolecular imaging. An enormous number of great discoveries have been achieved with the aid of fluorescence microscopy in studies of, e.g., cancer immunotherapy,[1] circadian clock,[2] autophagy,[3] induced pluripotent stem cells,[4] and calcium signaling.[5,6] In fluorescence microscopy, labeling of targeted molecules plays a key role. Specific and multiplex labeling of targeted molecules using various fluorescent probes allows the specific and sensitive imaging of multiple molecules and organelles simultaneously. In particular, the discovery of green fluorescent proteins[7] has revealed cellular activities in living cells in real-time format. However, labeling also limits this technique. Labeling probes, such as fluorescent proteins and organic dyes, are generally large and can change the properties of targeted molecules. Moreover, labeling techniques generally require long-term treatment, cell permeabilization, and/or cell fixation.

Raman microscopy is an emerging label-free molecular imaging modality for cell and tissue analysis.[8–12] In this Tutorial, we describe Raman microscopy with its instrumentation and applications in the molecular imaging of cells and tissues on the basis of published works.[8,12–16] A particular focus is made of slit-scanning Raman microscopy,[13] a high-speed hyperspectral Raman imaging technique that is widely applied to cell and tissue analysis.

II. LABEL-FREE MOLECULAR DETECTION BY RAMAN SCATTERING

When light interacts with a molecule, the optical field oscillates the electrons of the molecule, while the massive nucleus hardly moves. This electron oscillation relative to the static nucleus induces oscillating molecular polarization, which generates a dipole. The dipole emits secondary radiation as scattered light. Most of the scattering components have the same energy as the incident light and are called elastic scattering (or Rayleigh scattering), whereas a

portion of the scattered light has a different energy[14] and is called inelastic scattering. The gain and loss of energy of the molecule by inelastic scattering can be attributed to energy transfer between oscillated electrons and molecular vibrations. Inelastic scattering by molecular vibrations is known as Raman scattering. Figure 1 illustrates Raman and Rayleigh scattering processes.

The Raman effect was discovered as a new type of secondary radiation in 1928 by Chandrasekhar Venkata Raman and his colleague.[17] They also found in the year of the discovery that each substance displays a characteristic Raman scattering spectrum (namely, Raman spectrum), which can serve to identify it unambiguously.[18] This substance dependence of Raman spectra plays an essential role in Raman spectroscopy and microscopy for molecular identification in a sample without labeling.

Examples of Raman spectra and the corresponding chemical structures of biological molecules [D-glucose, glucose-6-phosphate (G6P) disodium salt, and glucose-1-phosphate (G1P) disodium salt] are shown in Fig. 2(a). These sugar molecules are precursors or intermediates of cell glycogenesis with similar chemical structures. Nevertheless, the spectra are clearly distinguishable. D-glucose does not have an intense band at ~970 cm^{-1}, whereas G6P and G1P disodium salts have sharp and intense bands attributable to the O–P–O vibrational mode at 976 and 965 cm^{-1}, respectively. G1P disodium salt has only one remarkable band at 845 cm^{-1} in the range of 350–900 cm^{-1}, whereas G6P disodium salt has three remarkable bands at 420, 500, and 820 cm^{-1} in the same range. In other ranges, the spectra of G6P and G1P disodium salts are distinct as well. The spectral differences between G6P and G1P disodium salts can be attributed to the difference in the position of the phosphate group on the ribose ring. These results clearly confirm that Raman spectroscopy is a powerful tool for identifying biological molecules specifically based on their intrinsic chemical structures.

Figure 2(b) shows the spectra of cytochrome *c* (cyt *c*), a molecule that plays key roles in biological activities such as ATP production and apoptosis. The redox state of cyt *c* is associated with its functions. Therefore, we demonstrated the redox sensitivity of Raman microscopy by measuring the Raman signatures of cyt *c* in

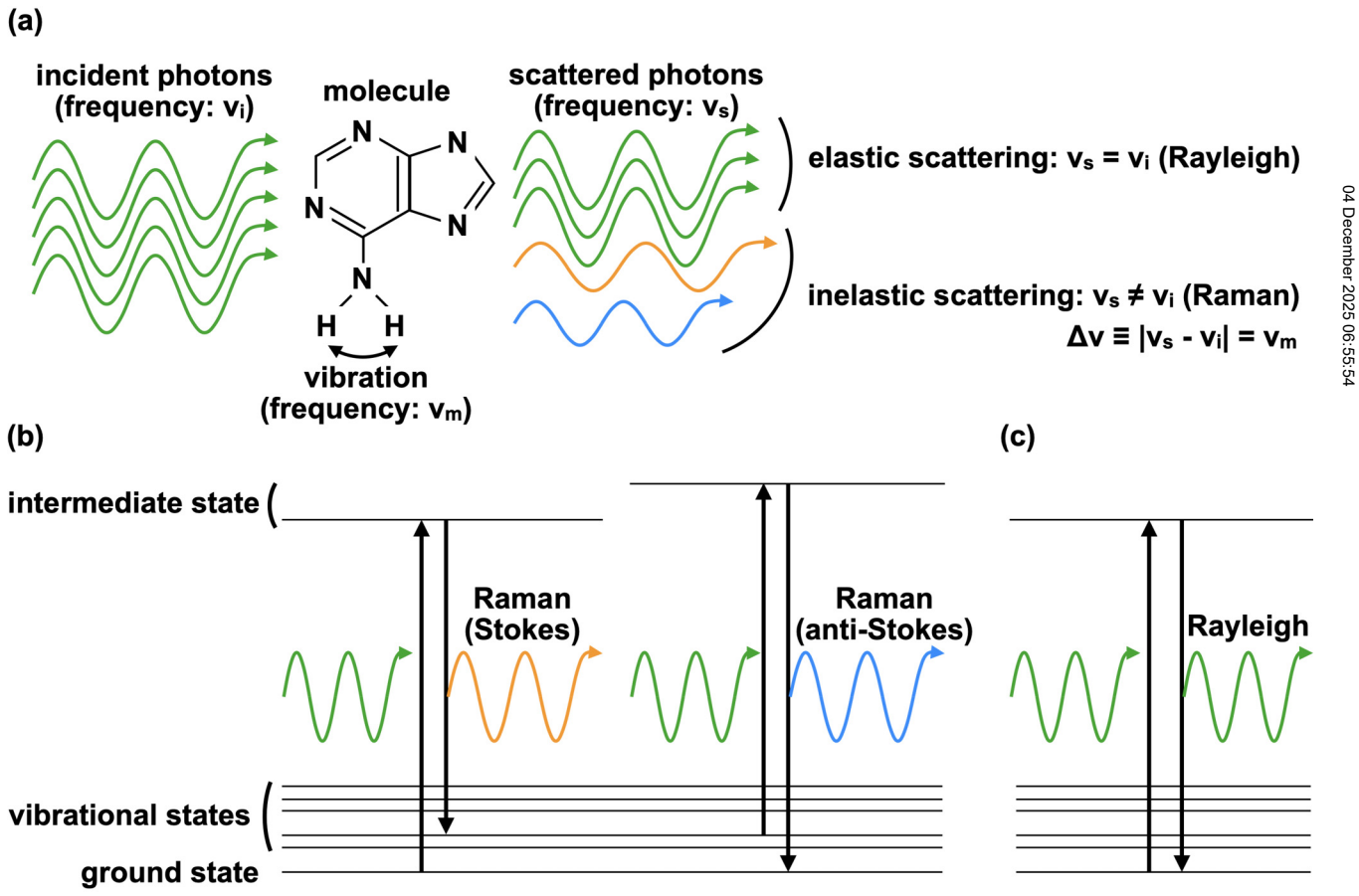

FIG. 1. Illustration of Raman scattering and Rayleigh scattering processes. (a) Phenomenalistic view of light scattering by a molecule with the relationship between the molecular vibration energy and the energy difference between a Raman scattering photon and an incident photon. (b) and (c) Energy diagrams of Raman scattering (b) and Rayleigh scattering (c).

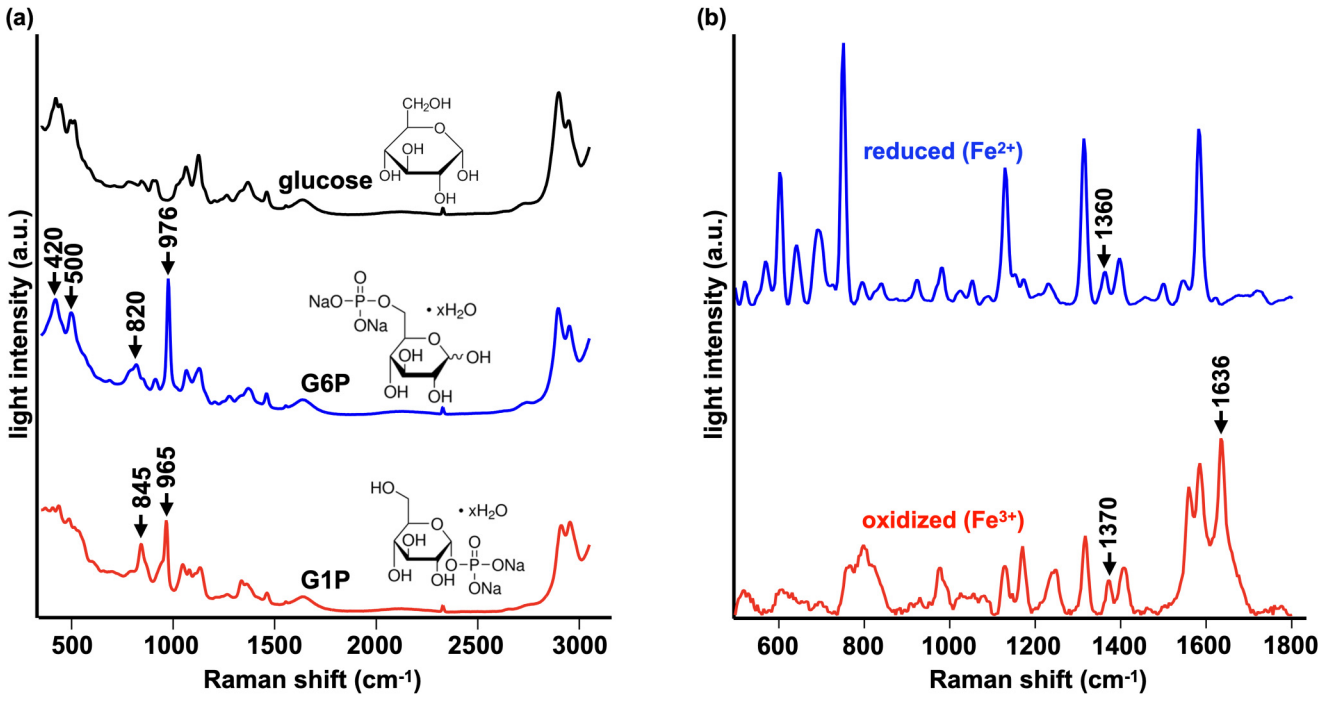

FIG. 2. Examples of Raman spectra and chemical structures of biological molecules. (a) D-glucose (top, black), glucose-6-phosphate (G6P) disodium salt (middle, blue), and glucose-1-phosphate (G1P) disodium salt (bottom, red) and (b) reduced (top, blue) and oxidized (bottom, red) forms of cyt *c*. The spectra were measured with a homebuilt Raman microscope equipped with a 532-nm excitation laser. The spectra in (a) are normalized by the intensity of the atmospheric nitrogen band at around 2330 cm^{-1}. The spectra in (b) were corrected in baseline and normalized by L2 norm.

the reduced form (ferrocytochrome *c* with Fe^{2+}) and the oxidized form (ferricytochrome *c* with Fe^{3+}). The heme *c* co-factor in the enzymatic pocket of cyt *c* resulted in resonance Raman scattering at 532 nm. The major vibrations originated from C—C, C═C, C—N, and C═N in porphyrin. The characteristic peaks of reduced cyt *c* include 750, 1125, 1310, and 1585 cm^{-1}. The oxidation of cyt *c* led to an overall decrease in the Raman intensity of wavenumbers listed above. The Raman marker bands of oxidation were defined at 1370 and 1636 cm^{-1}. In Fig. 2(b), a transition from 1360 to 1370 cm^{-1} and an appearance at 1636 cm^{-1} can be identified when compared to oxidized cyt *c* with reduced cyt *c*. This result is a good example of Raman microscopy detecting changes in the redox state of metalloproteins.

Raman spectra of a number of biological molecules have been measured in the last half-century.[12] Raman spectra databases of biological molecules are shared in the literature.[19–23] The Raman spectra databases are essential, particularly for analyzing samples that contain various molecular species, i.e., cells and tissues, because Raman spectra of such a sample can be a spectral ensemble of the molecules existing in the sample and, hence, be sophisticated.

III. CELL ANALYSIS BY RAMAN SCATTERING

The Raman spectrum of a cell is an ensemble of the Raman spectra of molecules present at the measurement site of that cell. We exemplify a cell Raman spectrum in Fig. 3. To distinguish the cellular components and non-cellular components (e.g., culturing substrate), the background spectrum measured in the same measurement conditions except for the absence of cell is also shown in the figure. Several spectral peaks are observed. Most of the peaks in the fingerprint region (400–1800 cm^{-1}) are assigned to cellular compositions, including cytochromes, proteins, lipids, and nucleic acids.

Similar to cyt *c* solution, the cell spectrum showed characteristic cytochrome peaks at 750, 1125, 1305, and 1585 cm^{-1} due to resonance Raman scattering excited at 532 nm. The shift from 1310 to 1305 cm^{-1} was due to *b*-type cytochromes in HepG2 cells. Another group of Raman shifts originates from proteins, the building blocks of cells, including phenylalanine (1000 cm^{-1}), amide-I (1680 cm^{-1}), amide-III (1250 cm^{-1}), and CH_2 bending (1450 cm^{-1}). Peaks can be assigned to adenine (725, 1340, and 1420 cm^{-1}), which is the building block of nucleic acids. In addition to cellular components, noncellular components, such as atmospheric gases and culture substrates, were also integrated.

In cell measurement, the signal intensity of a band depends on the Raman scattering efficiency and the quantity of molecules existing at the measurement site of the cell sample. Hence, molecules with large differential scattering cross sections and/or existing at high concentrations are generally measured. Protein is exceptional; although quantities of individual proteins are small in cells

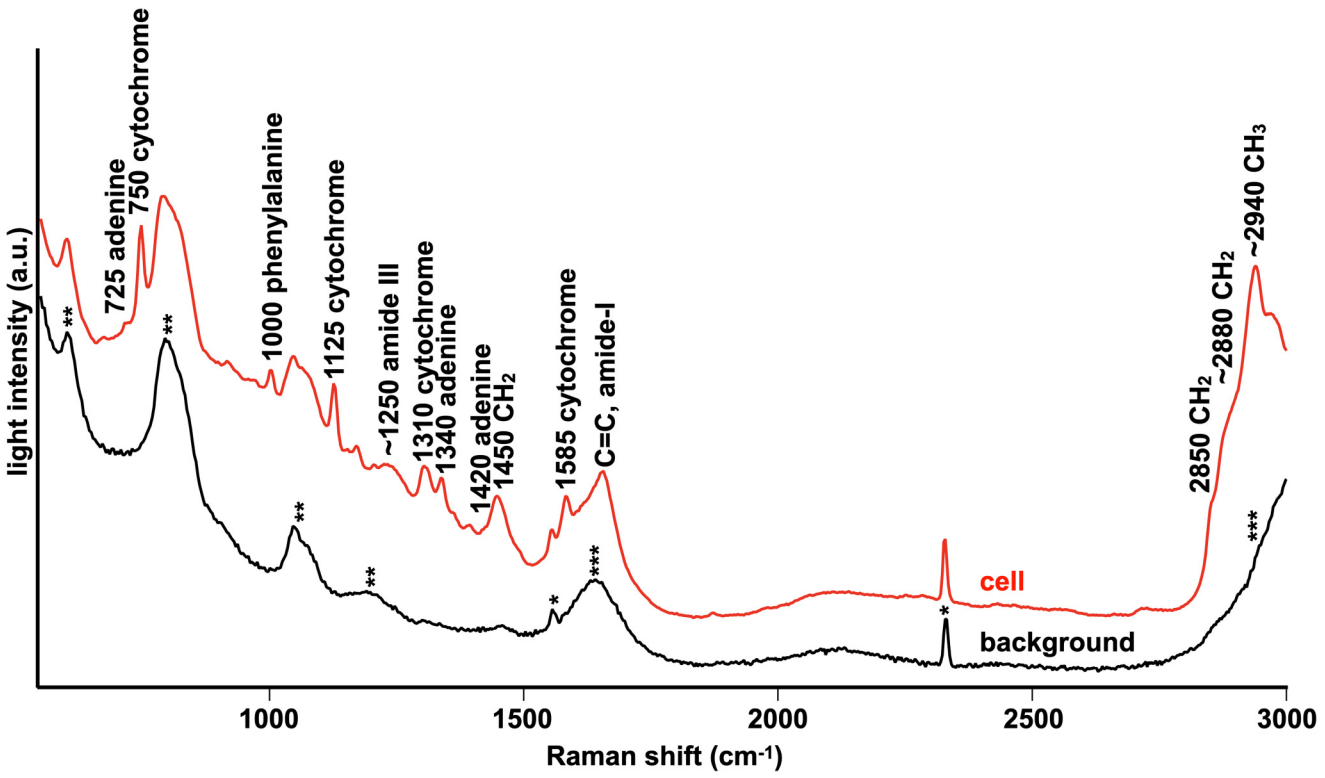

FIG. 3. Example of a cell Raman spectrum (red) and a background spectrum (black). The cell spectrum was measured from HepG2 cells, a cell line of human hepatocellular carcinoma, that was cultured on a quartz dish. The Raman scattering was accumulated from one single cell. The background spectrum was measured from the region without a cell in the culture dish. The excitation laser wavelength was 532 nm. Besides the cellular components, non-cellular components are seen, including atmospheric oxygen (~1550 cm^{-1}) and nitrogen (~2330 cm^{-1}) (⋆), and fused quartz of a cell culturing substrate and optical elements of the apparatus (~800 cm^{-1} and 1060 cm^{-1}) (⋆⋆), and water (~1635 and > 2800 cm^{-1}) (⋆⋆⋆).

and tissues, the total number of proteins are large and proteins are measured as an ensemble by their common structures, such as the peptide backbone and secondary structure.

The molecular composition varies among different cell types, and the Raman spectrum of the cell depends on the cell type. For example, red blood cells can exhibit remarkable bands of hemoglobin identical to those of cytochromes.[24] Two types of granulocytes, i.e., neutrophils and eosinophils, exhibit characteristic bands assigned to two hemoproteins, eosinophil peroxidase and myeloperoxidase, respectively.[25] Muscle cells can exhibit myoglobin bands besides cytochromes *b* and *c*.[26] Osteoblastic cells show an outstanding band of hydroxyapatite synthesized by the mineralization process.[27] Hepatic stellate cells, storing vitamin A in the body, can exhibit remarkable retinol bands in their Raman spectra.[28] Raman spectra can also depend on the cell state, e.g., degrees of healthiness and differentiation.

The molecules appearing in the Raman spectrum of the cell also depend on the excitation laser wavelength. When the excitation wavelength completely or closely matches the absorption band attributed to the electronic transition of a molecule, the electrons of the molecules oscillate in resonance with the optical field and a large dipole is induced at the molecule. Because the dipole emits Raman scattering as secondary radiation, the large dipole provides intense Raman scattering. Intense Raman scattering caused by electronic resonance is known as resonance Raman scattering. The resonance enhancement reaches four to six orders of magnitude and can even increase further. When the resonance condition is satisfied for specific molecules, they can be clearly measured in the cell Raman spectrum. As shown in Fig. 3, the Raman signals of cytochromes are enhanced in resonance with 532 nm excitation.

The resonance Raman effect is widely utilized in the Raman spectroscopy of cells and tissues. Figure 4 presents the excitation wavelength ranges commonly used for resonance Raman spectroscopy of cells and tissues. General protein constituents, such as peptides and amino acids, as well as nucleotide bases, such as adenine, guanine, thymine, cytosine, and uracil, are excited in the deep-ultraviolet (deep-UV) range for resonance Raman studies. In the visible range, heme proteins, such as cytochromes and hemoglobin, as well as retinoids and carotenoids, are excited for resonance Raman studies. The optimal excitation wavelength range for resonance Raman enhancement depends largely on the molecular structure.

The wavelength dependency of the cell spectrum due to the resonance effect must be properly considered in the interpretation

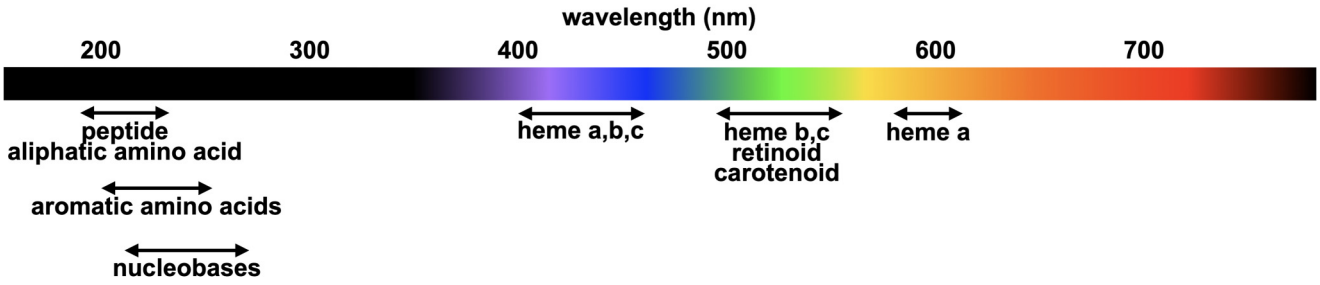

FIG. 4. Excitation wavelength range suitable for resonance Raman scattering of various biological molecules in cell and tissue.

of the cell spectra acquired in Raman measurements. Incorrect assignment of a Raman band can occur when the resonance effect is not properly considered for spectral interpretation.

IV. TISSUE ANALYSIS BY RAMAN SCATTERING

Similar to cells, tissues exhibit an ensemble Raman spectrum of all cells and extracellular matrix that exist at the measurement site. Figure 5 presents examples of tissue Raman spectra in the wavenumber range of 725–1800 and 2750–3090 cm^{-1}.[29] Skeletal muscle tissue, which is rich in heme proteins, exhibits remarkable bands assignable to reduced cytochromes *b* and *c* (746, 1124, 1309, and 1581 cm^{-1}) and deoxymyoglobin (1333, 1550, and 1603 cm^{-1}). Connective tissue, rich in collagen type I, which has characteristic secondary structures of proteins, exhibits a spectrum with characteristic amide-III and amide-I bands at 1241 and 1662 cm^{-1}, respectively. Adipose tissue, containing a large amount of oleic acid in animals, exhibits remarkable lipid bands assignable to oleic acids (1080, 1260, 1299, 1441, 1655, 1747, 2855, 2899, 2930, and 3004 cm^{-1}). The unmyelinated nerve, which is mainly composed of unmyelinated neural cells, exhibits a spectrum resembling the cell spectrum shown in Fig. 3. In contrast, the myelinated nerve, possessing a myelin sheath rich in sphingomyelin, exhibits feature bands assignable to sphingomyelin (1068, 1297, 1654, 1670, 2850, and 2885 cm^{-1}). Overall, the spectra reflect the molecular compositions of tissues; hence, they are different from each other.

The selection of excitation wavelength is more important in tissue measurements than in cell measurements because tissues contain more chemical components that show strong autofluorescence under laser irradiation, including fluorescent pigments. Specifically, in the case of visible wavelength excitation, autofluorescence hinders the Raman spectral measurement of the tissue. The autofluorescence is weaker at near-infrared excitation because endogenous pigments in tissue do not have remarkable absorption.[30] Hence, in tissue measurement applications, near-infrared lasers are widely used for Raman excitation.

Under deep-UV excitation, tremendously intense autofluorescence occurs.[31] Nevertheless, autofluorescence can be negligible when the excitation wavelength is down to 250 nm or shorter in deep-UV Raman spectroscopy.[32] In the excitation at such a short deep-UV wavelength, Raman scattering of biological molecules is generated at a wavelength region shorter than the wavelength of autofluorescence emission of the inherent molecules.[33]

In addition to excitation wavelength selection, several approaches suppressing the autofluorescence influence have been studied and developed in Raman spectroscopy, e.g., time-gating a detector to selectively reject fluorescence occurring with a delay to Raman scattering,[34] adding fluorescence quenchers in a sample,[35] subtracting two spectra measured at two slightly different excitation wavelengths,[36] separating polarized Raman scattering from little polarized fluorescence by a linear polarizer,[37] mathematically eliminating the fluorescent background from a measured spectrum,[30] and photochemically or chemically bleaching endogenous pigments.[38,39] However, a versatile method has not yet been established, and the possible autofluorescence is still the major issue in Raman spectroscopy of cells and tissues.

V. SLIT-SCANNING RAMAN MICROSCOPY

Cells contain various biomolecules. The spatial distributions of these molecules are not homogenous and are localized in different regions such as nuclei, mitochondria, and vesicles. In addition, tissues are more complex and heterogeneous because their distributions can vary among different cell types and cell states. To analyze cells and tissues in detail, imaging analysis is particularly helpful.

The principle of Raman imaging analysis is simple: Raman scattering from each finite region of a sample is measured independently, and a spatial distribution of the Raman spectra is obtained for the sample. However, the implementation of this principle is difficult because Raman scattering is extremely weak. A typical value of the differential Raman scattering cross section ranges from to 10^{-28} to 10^{-32} cm^2/steradian. These values are far smaller than the widely used absorption cross sections of fluorescent labels (i.e., 10^{-16}–10^{-17} cm^2).

The spatial distribution analysis of a living biological sample by Raman scattering spectroscopy was first demonstrated by Puppels *et al.* in 1990, 62 years after the discovery of the Raman effect.[40] In their study, it took 150 s or longer to acquire each spectrum due to weak Raman scattering. This long measurement time prevented two-dimensional high-resolution Raman imaging.

Scientists have made significant efforts to reduce the measurement time in Raman imaging. One of the major approaches for high-speed Raman imaging is multiplexing of spatial sampling.

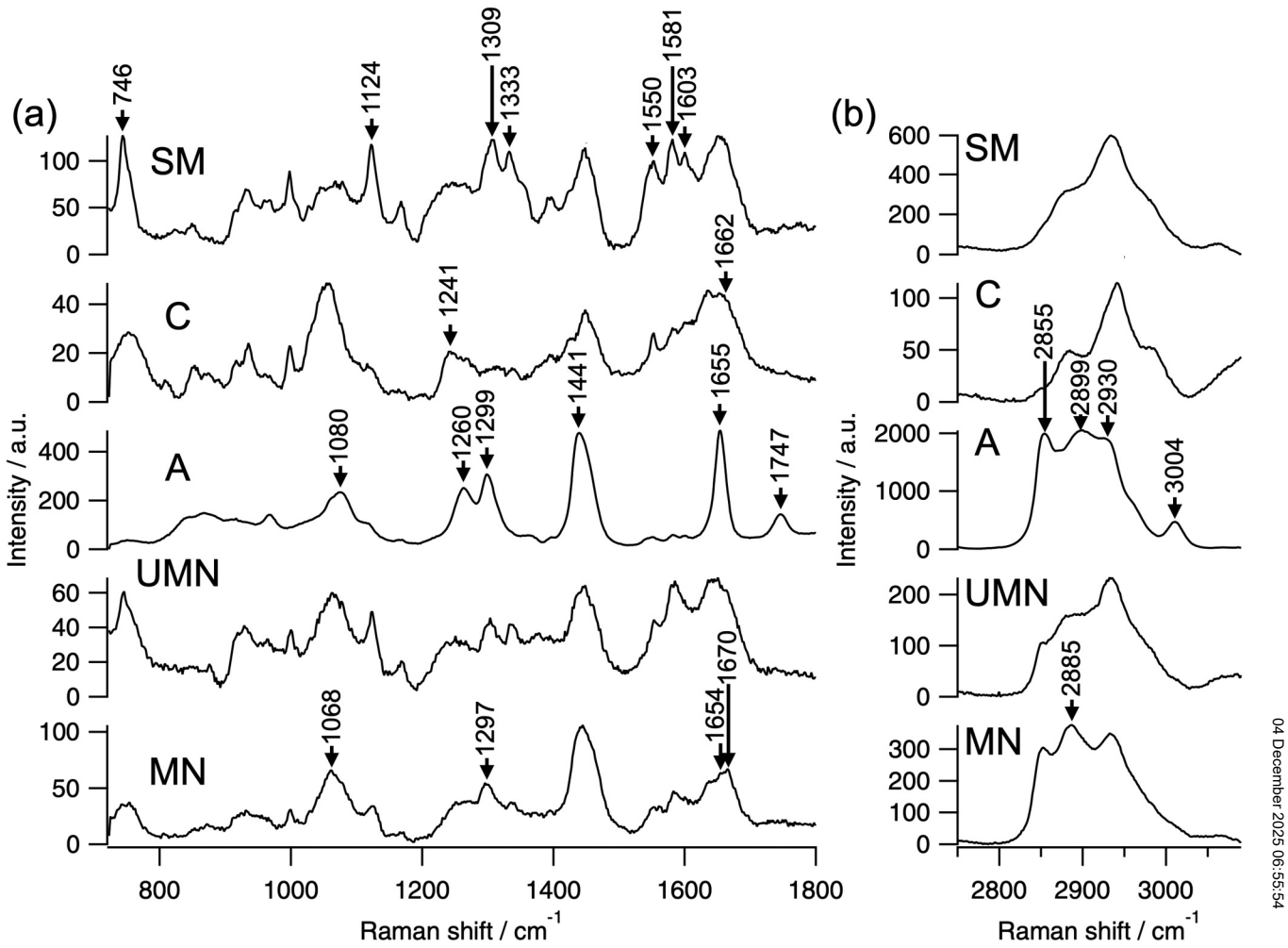

FIG. 5. Tissue Raman spectra measured from skeletal muscle tissue (SM), fibrous connective tissue (C), adipose tissue (A), unmyelinated nerve tissue (UMN), and myelinated nerve tissue (MN) extracted from rats. (a) 725–1800 cm^{-1}; (b) 2750–3090 cm^{-1}. Broad fluorescent backgrounds were removed with the use of a modified polynomial fitting. The excitation laser wavelength was 532 nm. Minamikawa *et al.*, Sci. Rep. **5**, 17165 (2015). Copyright 2015 Author(s), licensed under a Creative Commons Attribution (CC BY 4.0) license.

This Tutorial focuses on this approach, particularly slit-scanning Raman microscopy.[8,13]

Figure 6 shows a schematic of slit-scanning Raman microscopy that excites the Raman scattering of a sample using a line beam. Raman scattering in the excited region of the sample is focused on the entrance slit of a spectrophotometer equipped with a two-dimensional array detector. After light was dispersed in the spectrophotometer, it was detected as a one-dimensional hyperspectral Raman image (i.e., $x \times \lambda$ data) by the detector. To acquire a two-dimensional hyperspectral Raman image (i.e., an $x \times y \times \lambda$ data cube), the slit (or the line beam) scans the sample. Apparently, this process requires only one-axis scanning and consequently accelerates Raman imaging in comparison to the conventional confocal Raman microscope, which requires two-axis scanning.

The improvement of the imaging speed in slit-scanning Raman microscopy depends on the number of spectra contained in the one-dimensional hyperspectral Raman image. The maximum number of spectra is equal to the sensor number of the detector along the axis parallel to the slit. Because the sensor number is typically within the orders of 10^2–10^3, the Raman imaging speed can be increased by two or three orders of magnitude using slit-scanning Raman microscopy.

A slit-scanning Raman microscope is configured as shown in Fig. 7. A cylindrical lens is used to shape the excitation laser beam into a line beam. The line beam is relayed to the sample plane by lenses, including the objective lens. The same objective lens also collects the Raman scattering from the sample. The paths of the Raman scattering and the laser beam are separated using an edge

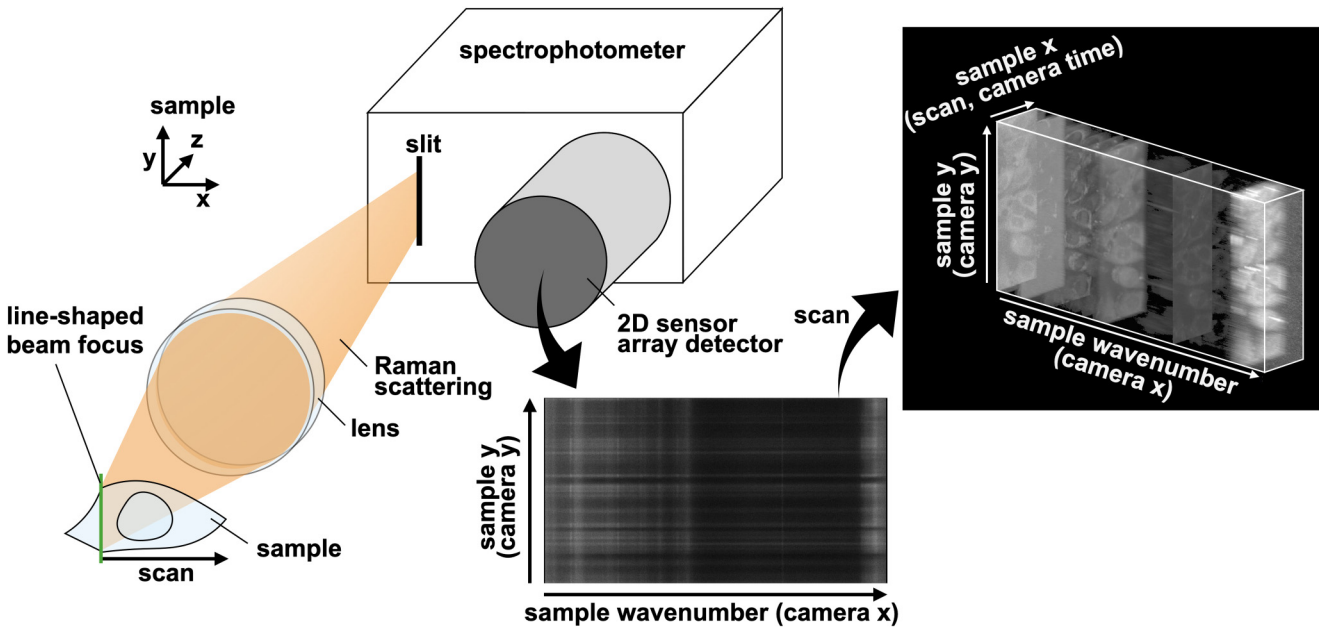

FIG. 6. Schematic illustration of slit-scanning Raman microscopy with illumination by a line beam.

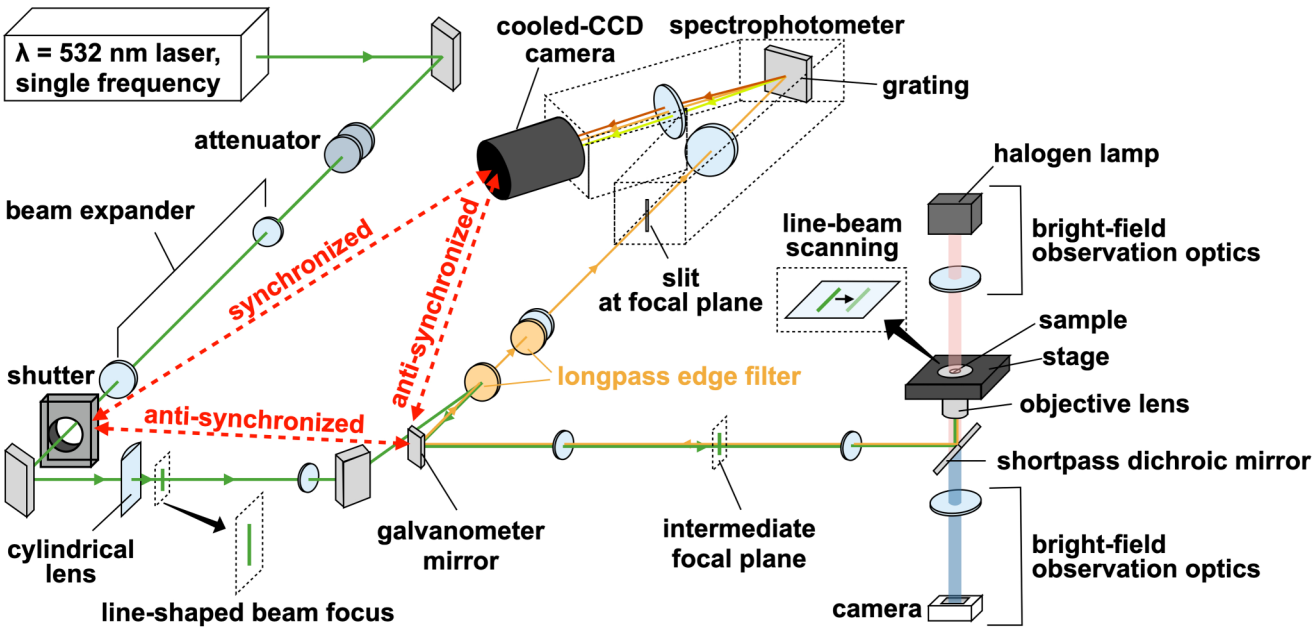

FIG. 7. Detailed optical setup of a slit-scanning Raman microscope. Besides the Raman imaging optics, the optical components for bright-field observation (i.e., halogen lamp, condenser lens, tube lens, and camera) are included. Light emitted from the halogen lamp passes through the shortpass dichroic mirror that reflects the laser beam and Raman scattering from the sample.

filter. Because the laser beam and elastic scattering light (i.e., Rayleigh scattering) are far more intense than Raman scattering, they are further rejected by another edge filter. Raman scattering passing through these filters enters a spectrophotometer equipped with a cooled CCD camera with a high quantum yield (~90% or even higher). Raman scattering is dispersed in the spectrophotometer and recorded by the CCD camera as a one-dimensional hyperspectral Raman image. The number of spatial sampling points in the one-dimensional image is determined by the line length and the number of sensors in the array detector. A two-dimensional hyperspectral Raman image is obtained by beam steering with the galvanometer mirror located in a Fourier plane.

The slit-scanning Raman microscope has several differences in optical configuration compared with the conventional confocal technique. The slit-scanning technique requires a high-power laser because the line-shaped beam focus has a larger area than the focused beam spot. A high-power laser allows the excitation intensity of the sample to be sufficiently high to acquire a large signal with a short accumulation time. The laser power of a slit-scanning Raman microscope is typically 1 W or higher. Because of the high laser power, beam power adjustment is often conducted using a combination of a half-waveplate and a linear polarizer but not using a neutral density filter.

The differences also include the use of a couple of cylindrical lenses as one-dimensional beam expanders. This one-dimensional beam expander adjusts the line length without affecting the beam width at the pupil of the objective lens. The beam width is adjusted using a traditional two-dimensional beam expander. With these two beam expanders, a tightly focused line beam with an arbitrary length is formed on the sample.

Compared with spot illumination, line illumination requires a larger laser power, whereas the intensity at the sample plane is equivalent. Therefore, the illumination intensity at locations other than the sample plane, e.g., at the sample substrate as well as at each optical component, is larger, and a larger amount of background light is generated from them in slit-scanning Raman microscopy. To reduce the background influence on the measurement, a fused quartz coverslip is used as a sample substrate because it has fewer fluorescent substances than typical optical glasses, such as BK-7 and SF-11. To further reduce the background, a special substrate such as a Raman-grade calcium fluoride substrate having no apparent Raman band except for a sharp peak at 321 cm^{-1}, is used.[8,41] Polished stainless substrate was also proposed to reduce the background from a sample substrate in Raman spectroscopy of cells and tissue.[42]

In addition to the aforementioned configuration, other configurations, e.g., using a Powell lens for generating a line-shaped beam focus laser[43] and a translation stage for scanning,[44] are available for implementing a slit-scanning Raman microscope.

VI. LIVE-CELL IMAGING APPLICATIONS

A major advantage of the slit-scanning technique over conventional confocal Raman microscopy is its imaging speed. A fast imaging technique is helpful for observing a moving object, such as a living cell. Hamada *et al.* presented live-cell imaging by slit-scanning Raman microscopy in 2008 for the first time.[13] They demonstrated a movie showing the dynamics of cyt *c*, protein, and lipid upon mitotic division of HeLa cells. One frame was taken at 185 s, and the frame interval was 5 min.

Since the first work was published, various studies have demonstrated the utility and potential of slit-scanning Raman microscopy in live-cell imaging and analysis. Drug uptake processes were observed in cancer cells without labeling of any molecule.[45] Spatiotemporal biochemical changes in single lymphocytes exposed to drug were quantified.[44] Apoptotic cells were observed in a time-lapse manner, and it was revealed that cyt *c* is kept at the reduced state through the release process from mitochondria.[41] Osteoblast mineralization processes were monitored with time-lapse Raman imaging of cyt *c*, hydroxyapatite, and β-carotene.[46] Cancer cells were discriminated from non-cancerous epithelial cells by unsupervised machine learning analysis of high-resolution hyperspectral Raman image data.[47] These works could not be realized by conventional confocal Raman microscopy.

Figure 8 presents a live-cell image of HepG2 obtained by slit-scanning Raman microscopy. Representative spectra are shown in Fig. 8(a), and the Raman images reconstructed by the band intensities of CH_2 symmetric stretching at 2850 cm^{-1}, porphyrin ring breathing at 750 cm^{-1}, and amide-I at 1680 cm^{-1} are shown in Fig. 8(b). The CH_2 symmetric stretching band represents the lipid distribution in cells, highlighting lipid droplets. The porphyrin ring breathing band, enhanced by the resonance effect at 532 nm excitation, represents the distributions of cytochromes *b* and *c* and is localized in the cytoplasm. The amide-I band, which reflects the protein secondary structures, represents the ensemble distribution of proteins in cells. The amide-I band vaguely visualizes nucleoli that are dense in molecules and can be identified in the bright-field image.

To prepare a living cell sample for Raman imaging, cells were grown in a culture medium containing nutrients, growth factors, and phenol red. Many contents in the culture medium can increase the background of the Raman measurements. Before Raman measurement, the culture medium is generally replaced by a buffer solution that does not contain fluorescent substances or organic substances, such as aromatic amino acids and proteins. The replacement of culture medium is the only pretreatment that is often required for Raman imaging measurements to reduce background noise.

VII. TISSUE IMAGING APPLICATIONS

A fast imaging technique is also useful for measuring a fresh sample that degrades over time, such as biological tissue excised from the body. Ogawa *et al.* applied the slit-scanning Raman imaging technique to biological tissue measurement for the first time in 2009.[48] They analyzed fresh heart tissue excised from intact rats and distinguished cardiomyocytes, arteries, and veins by resonance Raman scattering of cytochromes (*b* and *c*), oxyhemoglobin, and deoxyhemoglobin. They also analyzed infarcted myocardial hearts excised from rats and discriminated intact cardiomyocytes and fibrotic tissue based on the signals of cytochromes and type-I collagen.

Biological tissues are often fixed using chemical and physical methods prior to Raman imaging for subsequent analyses by, e.g.,

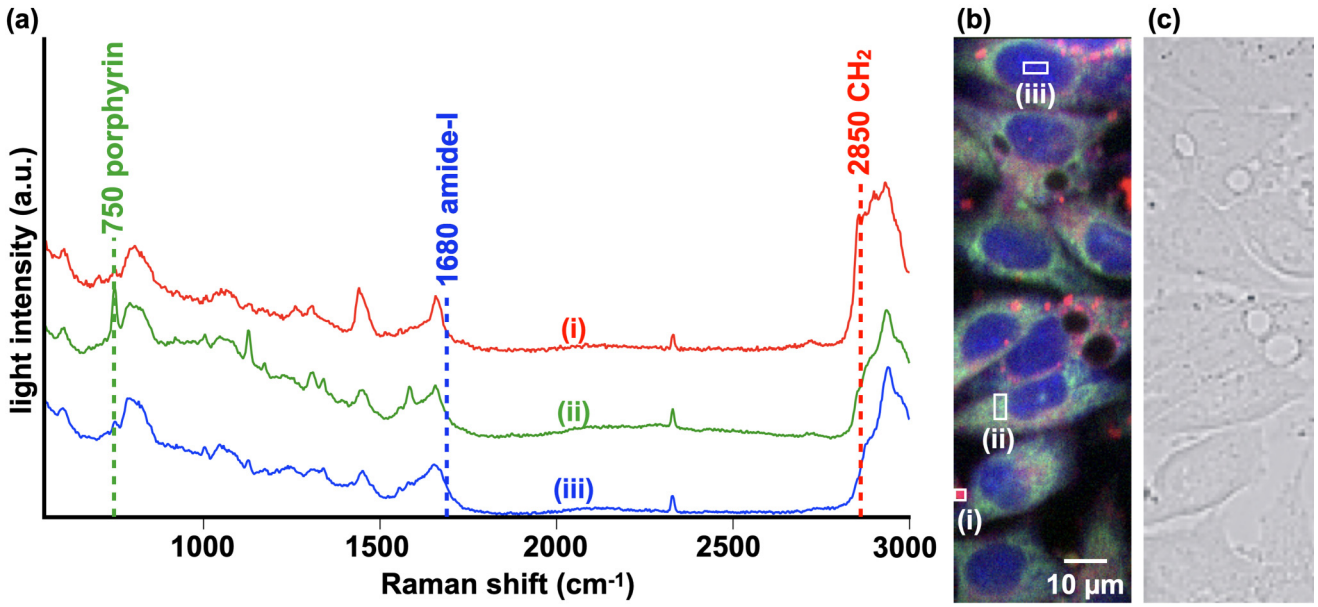

FIG. 8. Live-cell imaging result of HepG2 by slit-scanning Raman microscopy. (a) Representative spectra and (b) Raman image. The representative spectra (i), (ii), and (iii) in (a) resulted from averaging over the regions indicated by (i), (ii), and (iii) in (b), respectively. The colors red, green, and blue in (b) represent the Raman band intensities of 2850 cm^{-1} CH_2 symmetric stretching, 750 cm^{-1} porphyrin breathing, and 1680 cm^{-1} amide-I vibration, respectively. Prior to image reconstruction, broad fluorescent backgrounds were removed with the use of a modified polynomial fitting and noise components in the data were removed using a singular value decomposition process. (c) Bright-field image of the cells shown in the Raman image (b). The cells were cultured on a fused quartz substrate thinly coated with collagen and immersed in a buffer solution upon measurement. The imaging plane was at 3 μm apart from the substrate. The excitation laser wavelength was 532 nm. The laser power was 3 mW/μm^2. The signal accumulation time per acquisition was 5 s/line. The image size is 400 × 126 pixels. The objective lens used was 40×/1.25 w of Nikon.

immunochemistry and histopathology. Even after fixation, molecules and cells in the tissue can be degraded in hours or days, and fast imaging by slit-scanning Raman microscopy is also beneficial. Infarcted perfused myocardium was analyzed and intact, necrotic, and granulation tissue at the border between infarcted and intact regions was distinguished by Raman spectral features.[49] Human tissue resected during myocardial infarction surgery was also studied, and the infarct border zone was identified.[50] Besides heart tissue, peripheral nerve tissue was also studied by slit-scanning Raman microscopy. On Raman images, peripheral nerves were distinguished from adjacent tissues such as adipose tissue, fibrous connective tissue, and skeletal muscle tissue not only in rat tissue but also in human tissue.[51] Peripheral nerves with and without myelin sheaths, i.e., myelinated and unmyelinated nerves, were also distinguished.

Figure 9 shows the tissue imaging results of the mouse brain hippocampus obtained by slit-scanning Raman microscopy. Representative spectra are shown in Fig. 9(a), and the Raman images reconstructed by the band intensities of CH_2 symmetric stretching at 2850 cm^{-1}, C═C stretching at 1520 cm^{-1}, and CH_3 anti-symmetric stretching at 2940 cm^{-1} are shown in Fig. 9(b). The CH_2 symmetric stretching band and CH_3 anti-symmetric stretching band clearly reconstructed the characteristic histology of the brain hippocampus dentate gyrus composed of polymorphic layer, molecular layer, and granular cell layer. The C═C band, localized in the brain sample, was attributed to carotenoids, together with the C—C band at 1155 cm^{-1}. The detection of carotenoids in brain tissue by Raman scattering is consistent with previous studies.[52,53] Carotenoids are targets for the study of brain inflammation as they have antioxidant and anti-inflammatory effects[53] and can accumulate at inflamed sites such as amyloid-β plaques.[54] Slit-scanning Raman microscopy, enabling fast label-free molecular imaging of brain tissue with a large field of view, can be helpful for studying brain inflammation, e.g., in Alzheimer's disease.

VIII. FASTER IMAGING BY ADVANCED TECHNIQUES

The total data acquisition time of Raman imaging includes not only the signal accumulation time but also the sensor readout and beam steering times. The signal accumulation and beam steering times are proportional to the scan number, whereas the sensor readout is proportional to the number of sensors used to record all the spectra. Thus, the sensor readout time is not reduced in slit-scanning Raman microscopy compared with conventional confocal Raman microscopy.

The sensor readout rate depends on the sensor type and readout voltage. In cooled CCD cameras that are widely used in Raman microscopy, the sensor readout rate ranges from several tens of kilohertz to several megahertz. At these readout rates, a single spectral readout with approximately a thousand sensors

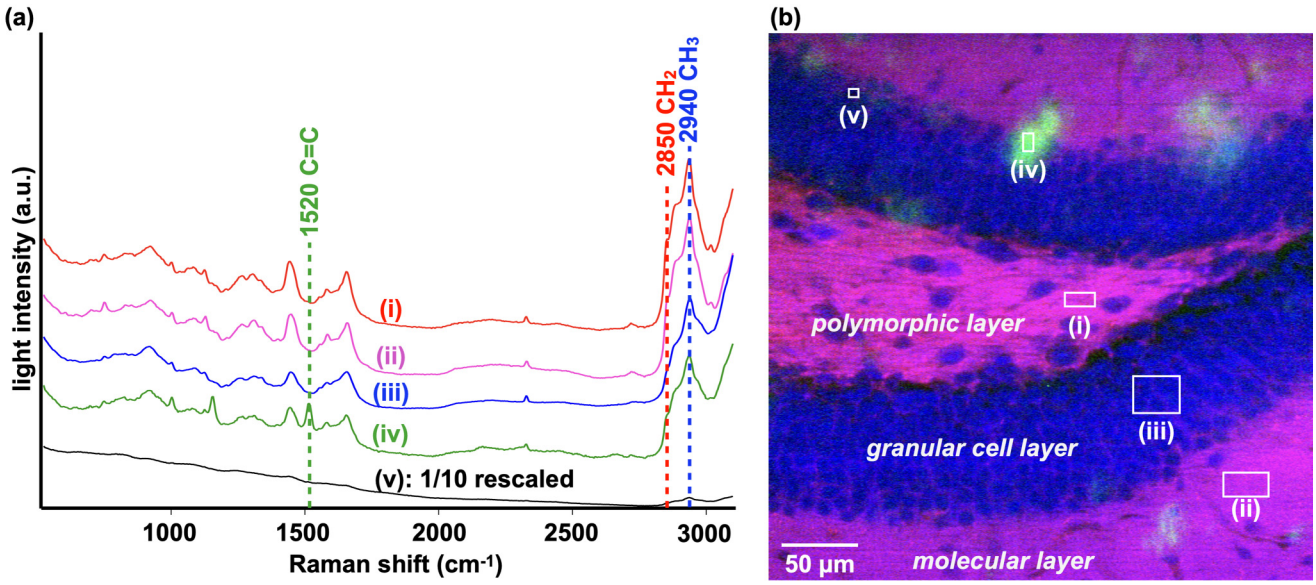

FIG. 9. Tissue imaging result by slit-scanning Raman microscopy. (a) Representative spectra and (b) Raman image. The representative spectra (i), (ii), (iii), (iv), and (v) in (a) resulted from averaging over the regions indicated by (i), (ii), (iii), (iv), and (v) in (b), respectively. The colors red, green, and blue in (b) represent the Raman band intensities of 2850 cm^{-1} CH_2 symmetric stretching, 1520 cm^{-1} C═C stretching, and 2940 cm^{-1} CH_3 anti-symmetric stretching, respectively. Prior to image reconstruction, broad fluorescent backgrounds were removed with the use of a modified polynomial fitting and noise components in the data were removed using a singular value decomposition process. The sample was mouse brain tissue fixed with paraformaldehyde and cryo-sectioned prior to measurement. All the animal care and handling procedures were approved by the Animal Care and Use Committee of Osaka University (Approval No. 28-1). The excitation laser wavelength was 532 nm. The signal accumulation time per acquisition was 3 s/line. The image size is 800 × 399 pixels. The objective lens used was 25×/1.1 w of Nikon.

often takes several hundred microseconds to several tens of milliseconds.

Figure 10 plots signal accumulation and readout times to the number of spectra simultaneously acquired per exposure in parallel by multiplex spatial sampling. In conventional confocal Raman microscopy where only one spectrum is acquired per exposure (i.e., "number of spectra per exposure" = 1 in Fig. 10), the sensor readout time is shorter by two to four orders of magnitude than the signal accumulation time and, hence, is ignorable. On the other hand, in slit-scanning Raman microscopy where hundreds of spectra or even more spectra are acquired per exposure, the sensor readout time can be equivalent to or even longer than the signal accumulation time. Hence, the imaging speed of slit-scanning Raman microscopy is affected not only by the signal accumulation time but also by the sensor readout time.

Reduction in the readout time further accelerated Raman imaging in the slit-scanning technique.[14] The readout time reduction relied on narrowing the spectrum detection range from ~2500 cm^{-1} to ~100 cm^{-1} while all other experimental conditions were maintained. With this narrowband detection, the number of sensors used to record each spectrum was reduced to 50. This sensor number is 24-fold smaller than the sensor number used for conventional wideband detection measuring the molecular fingerprint region (600–1800 cm^{-1}), silent region (1800–2800 cm^{-1}), and CH region (2800–3100 cm^{-1}). Hence, a 24-fold reduction in the sensor readout time was achieved using the narrowband detection method.

A higher readout rate can also reduce readout time. However, a higher readout rate requires a higher readout voltage, which causes larger readout noise. A large readout noise lowers the signal-to-noise ratio (SNR) in the measurement, similar to the short signal accumulation time. The signal accumulation time needs to be extended for the SNR to be maintained; consequently, the imaging time cannot be effectively shortened.

The measurement acceleration by the narrowband detection method was quantified using live-cell Raman imaging.[14] The readout rate of the CCD camera was 100 kHz. To acquire a single spectrum, the narrowband detection method using 50 sensors for spectral recording took 0.5 ms, while the conventional wideband detection method using 1200 sensors took 12 ms. The signal accumulation time was 3 s for a multiplexed acquisition of 1200 spectra by line illumination, and hence, the effective signal accumulation time for each spectrum was 2.5 ms (=3/1200). To sum up, the time in acquiring each spectrum was 3.0 and 14.5 ms for narrowband and wideband detection methods, respectively. The narrowband detection method was five times faster than the conventional wideband method. Acquiring 1200 × 250 hyperspectral Raman images of MCF-7 cells took only 15 min using the narrowband detection method.

Further acceleration of Raman imaging is achieved by applying binning to the sensor array. The binning process, which integrates multiple neighboring sensors as a single sensor, reduces the number of effective sensors and, hence, reduces the sensor readout

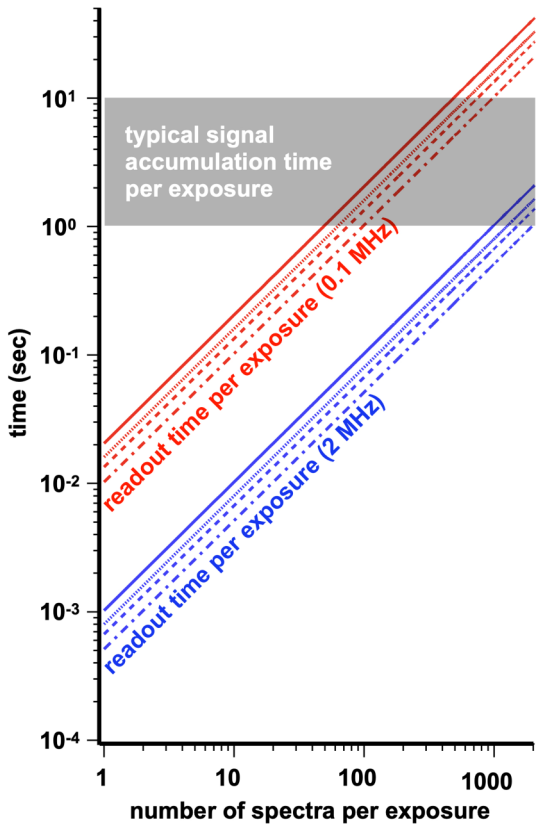

FIG. 10. Signal accumulation and readout times per exposure in multiplex spatial sampling. The values are plotted to the number of the spectra simultaneously acquired per exposure in parallel. We considered typical experimental conditions and assumed signal accumulation times of 1–10 s, detector readout rates of 0.1 and 2 MHz, and wavenumber points of 1024, 1340, 1600, and 2048 for each spectrum. Solid lines, dotted lines, dashed lines, and dashed dotted lines correspond to the wavenumber points of 2048, 1600, 1340, and 1024, respectively.

time. By applying the binning process to four serial sensors in the spectral axis, the acquisition time for the narrowband detection method of MCF-7 Raman imaging under above conditions was further reduced from 15 to 2.5 min.

The low spectral resolution measurement benefited from the photon number incident on an effective sensor. The number of photons incident on an effective sensor after the binning process was larger than that incident on an individual sensor before the binning process. Thus, with the binning process, the signal accumulation time was shortened without sacrificing the signal level. Figure 11(a) presents the narrowband and low-resolution Raman imaging results of living cells measured with the signal accumulation time of 0.7 s.[14] Each of the Raman images, consisting of 1200×1500 (1.8 M) pixels, was acquired in only 21 min. This acquisition time was 21-times faster than the time required for conventional wideband and high spectral resolution measurements using slit-scanning Raman microscopy. Nevertheless, the SNR of the images was approximately twofold higher in narrowband and low-resolution measurements.

Spectral information is a trade-off with the speed brought about by low spectral resolution and narrowband measurement. However, the loss of spectral information does not cause a critical problem, depending on the application. Figure 11(b) shows results of principal component regression analysis using narrowband and low-resolution spectra of 100 cancer cells and 100 non-cancer cells at 1397–1501 cm^{-1} with 13 wavenumber points (~8 cm^{-1}/wavenumber point).[14] In the results, the cancer cells were distinguished from non-cancer cells with an accuracy of 90.5%. This accuracy was similar to that derived from the wideband and high-resolution spectra (93.8%). As another example, Schie *et al.* examined various spectral resolutions in three cell line classifications by Raman spectroscopy and reported that the spectral resolutions of 8 and 64 cm^{-1} did not show a remarkable difference in accuracy of the classification of three cancer cell lines, Jurkat, MiaPaca2, and Capan1 (93.3% at 64 cm^{-1} and 95.3% at 8 cm^{-1}).[55] Additionally, Duraipandian *et al.* revealed that in the classification analysis, the accuracy of the diagnosis of skin cancer was improved using specific wavenumbers instead of total wavenumbers.[56]

Limiting the "spatial" information also accelerates slit-scanning Raman imaging. Spatial information is reduced either by reducing the measurement area/volume or by reducing the sampling lines over a constant area/volume. Among these, the latter approach can hardly lose spatial information when it is followed by data reconstruction using a mathematical approach. Pavillon and Smith applied a compressed sensing algorithm to a subsampled image of living cells acquired by slit-scanning Raman microscopy.[57] With 20% subsampling (i.e., fivefold faster sampling) and data reconstruction constrained by total variation minimization of the reconstructed data, little significant loss was found in the cell structural information. In addition, the total variation minimization reconstruction improved the SNR owing to the mathematical process, allowing the signal accumulation time to be set shorter. Hence, compressed sensing slit-scanning Raman microscopy achieved 10-times faster measurement without significantly sacrificing the spatial information in comparison to the original slit-scanning Raman microscopy.

IX. VIBRATIONAL TAGS FOR SPECIFIC MOLECULAR IDENTIFICATION

Even though the measurement speed was increased by slit-scanning Raman microscopy, there is still a limitation in Raman imaging for biomedical applications, which is the difficulty in the specific identification of the targeted molecules. In the Raman spectrum of cells or tissues, intracellular molecular bands overlap. Therefore, it is often difficult to identify the Raman band assigned to a single molecular species unless a specific molecular species is enhanced by the resonance effect,[8,13,41,46,48] is externally introduced,[45] or exists at an extremely high concentration.[58]

A molecule with a characteristic band can be identified from the Raman spectrum of a cell or tissue. Vibrational tags have been proposed as chemical structures that rarely exist in cells and tissues and can be distinguished from intrinsic molecules. Vibrational tags can be identified specifically due to a characteristic band in the silent region, where no apparent cell or tissue signal appears. The concept of vibrational tag Raman imaging was first demonstrated

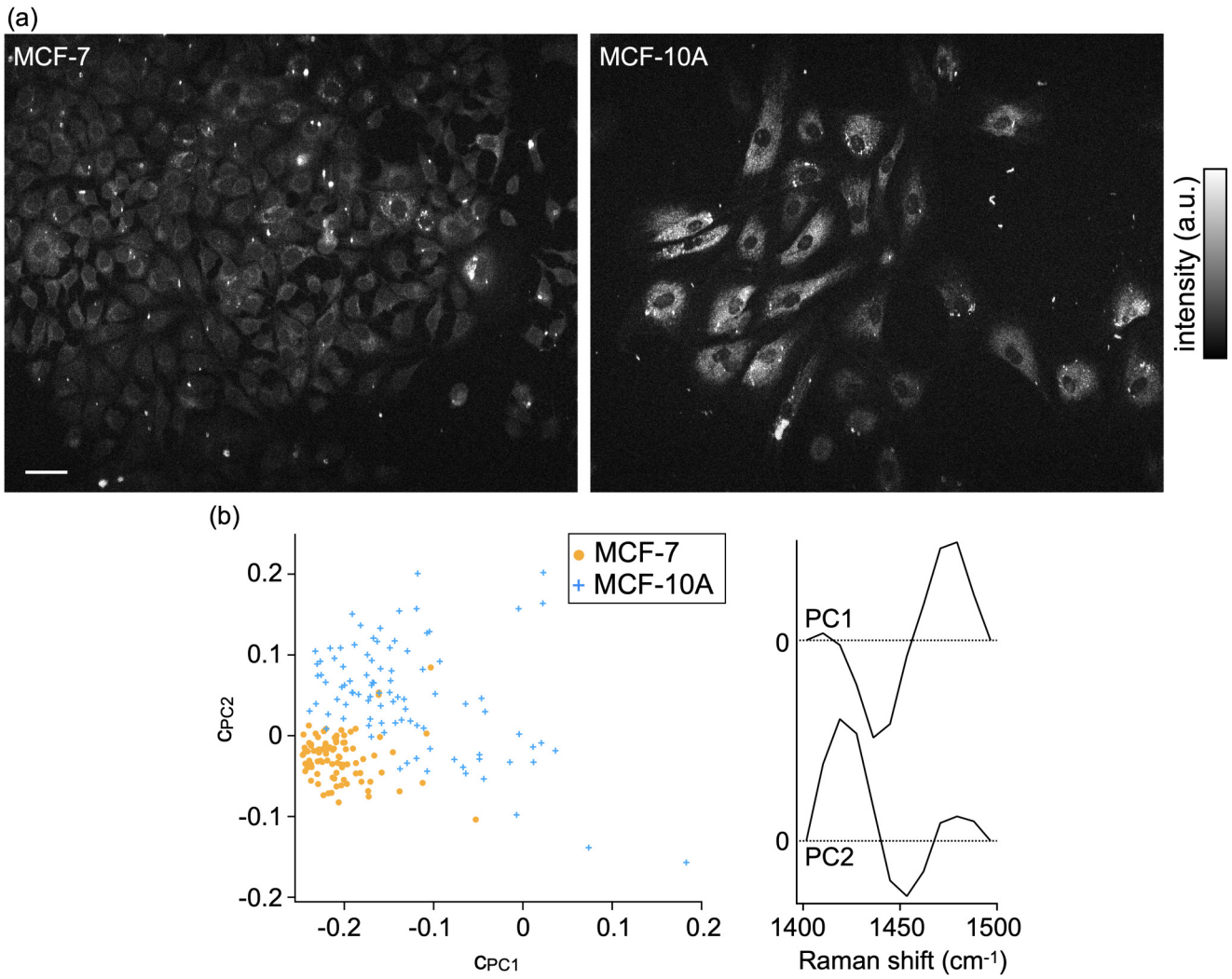

FIG. 11. Narrowband and low-spectral-resolution Raman imaging acquiring 1397–1501 cm^{-1} spectral range with 13 effective sensors. Human mammary gland cell lines, MCF-7 and MCF-10A, were measured. (a) 1200 × 1500 pixels Raman images reconstructed by the average intensity of 1432–1458 cm^{-1} attributed to CH_2 vibration. The scale bar shows 50 μm. (b) Results of principal component and regression analysis using narrowband and low-resolution spectra of 100 MCF-7 and 100 MCF-10A cells. The regression coefficients to the first and second loadings, c_{PC1} and c_{PC2}, are plotted for all the 200 cell cytoplasm spectra. The first and second loadings are also shown. Reproduced with permission from Kumamoto *et al.*, J. Phys. Chem. B **121**, 2654 (2019). Copyright 2019 American Chemical Society.

in 2011 by Yamakoshi *et al.* with the use of a slit-scanning Raman microscope.[59] They used EdU, an alkyne-tagged cell proliferation probe. EdU has a specific Raman band at 2122 cm^{-1} assigned to the alkyne (—C≡C—). After EdU was incorporated into the nucleic acid instead of thymidine during the cell proliferation, it was detected in the cell nuclei by the alkyne Raman band.

Figure 12 shows EdU-incorporated living cells measured by slit-scanning Raman microscopy. The 2122 cm^{-1} band characteristic to EdU appears clearly only at nucleoplasm, where DNA, deoxyribonucleic acid, is synthesized. Because the EdU band appears in the silent region and hardly overlaps with any other band, the image reconstructed by the alkyne band intensity clearly represents the EdU distribution in the cells. On the other hand, EdU does not clearly affect the Raman images of endogenous molecules because EdU has only one remarkable band other than at 2122 cm^{-1}, i.e., around 1620 cm^{-1}.[59]

Fluorescence is another (and more popular) approach to the detection of EdU incorporated in living cells. However, fluorescent detection requires a click reaction, in which fluorescent azide is bound to an alkyne. This reaction hinders the real-time detection of EdU and creates other complications, such as the reaction rate of alkynes with fluorescent azides. Direct probing of alkynes using the fast Raman imaging technique allows real-time and quantitative observation of the cell proliferation.

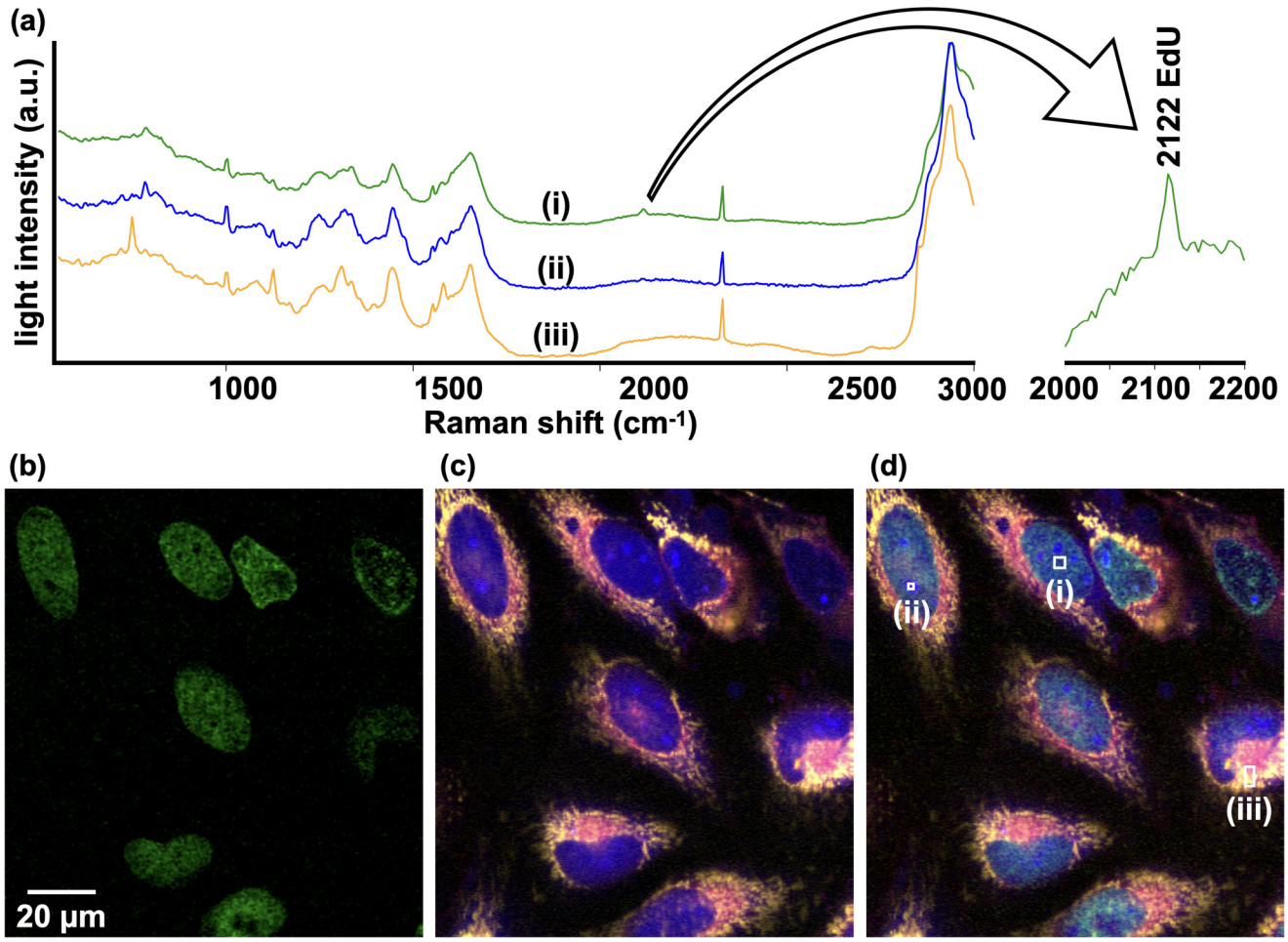

FIG. 12. EdU-incorporated living HeLa cells measured by slit-scanning Raman microscopy. (a) Representative spectra of nucleoplasm, nucleoli, and cytoplasm from top to bottom. (b)–(d) Raman images representing the distributions of (b) EdU (2122 cm^{-1}), (c) lipid (red, 2850 cm^{-1}), protein (blue, 2940 cm^{-1}), and cyt *c* (yellow, 750 cm^{-1}), and (d) all in (b) and (c) together. Each spectrum in (a) was taken from each of the regions indicated in (d).

Raman imaging of EdU was performed to demonstrate the capability of small molecules to be imaged using vibrational tags. Compared to deoxyuridine, the original nucleobase with $-CH_3$, EdU was only 4.0% heavier. This subtle difference in the molecular structure and weight minimizes its influence on biological activity. Small molecules that cannot be labeled with large organic fluorescent substances with π-conjugation in the molecular structure, and thus are large in general, can be visualized by Raman tag imaging.

Alkyne has a relatively large Raman scattering cross section and has been widely studied for vibrational tag Raman imaging. Various alkyne groups with different side chains,[60] conjugation lengths,[60,61] carbon isotopes (^{12}C, ^{13}C),[61] and hydrogen isotopes (H, D)[62] have been studied, and Raman-tag probes with alkyne groups have been developed for specific organelle labeling.[61,63] Alkyne-tag Raman imaging has recently been reviewed in the literature.[64]

In addition to alkynes as Raman tags, various vibrational groups have been explored and nitrile ($-C{\equiv}N$) and deuterium ($-D$) have also been utilized as Raman tags. A nitrile tag was used to monitor two different states of a chemical substance, protonated and deprotonated carbonylcyanide p-trifluoromethoxyphenylhydrazone (FCCP) in a living cell, as it shows the spectral shift in the nitrile band of FCCP depending on protonation/deprotonation.[65] A deuterium tag was used in the study of biological metabolism because deuterium, a single atom, can be moved from one molecule to another through a metabolic process.[66]

X. SELECTIVE ENHANCEMENT OF RAMAN SCATTERING

A small number of molecules cannot be identified in the spectrum of cells or tissues, even if the molecules have a characteristic Raman band. In many cases, Raman scattering of such molecules cannot be recognized in a spectrum composed of a variety of intracellular molecules. Selective enhancement of Raman scattering

helps identify molecules at low concentrations. The resonance Raman effect is one such selective enhancement approach.

Surface-enhanced Raman scattering (SERS) by metallic nanoparticles allows selective Raman enhancement of molecules present at low concentrations because it occurs only for the molecules existing in the vicinity of the particles.[33] Schematic illustrations of the SERS effect and the selective Raman enhancement by SERS are shown in Fig. 13. SERS was used for detecting a small amount of drug substances incorporated in living cells by slit-scanning Raman microscopy.[15] The cells were first incubated with gold nanoparticles (GNPs) so that the nanoparticles were incorporated and accumulated into lysosomes by endocytosis and worked as SERS probes. Alt-AOMK, a cathepsin B inhibitor with an alkyne, was then added to the cell culture medium. Alt-AOMK is also destined for lysosomes, where the lysosomal cysteine protease cathepsin B exists. When the drug substance reached near the GNPs within the lysosome, an SERS signal of the alkyne was generated, allowing selective detection of drug molecules in living cells. Drug uptake was measured using three-dimensional time-lapse imaging by slit-scanning Raman microscopy. Each frame was taken only in 21 s/volume, owing to the SERS effect and the slit-scanning fast acquisition, as well as the precise and fast z-steering of the objective lens by a piezo-electric stage. Figure 14 shows representative frames of the three-dimensional time-lapse imaging movie. The drug substances incorporated into the lysosomes are indicated in green by alkyne SERS intensity. The existence of GNPs in cells was confirmed by the intensity distribution of SERS attributed to endogenous molecules (shown in red). From these results, the authors succeeded in monitoring the gradual drug uptake process.

Zhang *et al.* presented *p*H sensing in living cells with SERS imaging by slit-scanning Raman microscopy.[67] They conjugated GNPs with para-mercaptobenzoic acid, p-MBA, and *p*H-sensitive molecules and incorporated the conjugated nanoparticles in living HeLa cells through membrane permeabilization by electroporation. Two SERS bands assigned to COO⁻ and C═O stretching modes of p-MBA were identified in the cell spectra. The intensity ratio of these two peaks was used to quantify the local intracellular *p*H near the nanoparticles. Owing to the SERS effect, fast time-lapse *p*H sensing using slit-scanning Raman microscopy was enabled, and a decreasing trend in intracellular *p*H during apoptosis was observed.

SERS imaging can also be applied to various types of functional sensors. Puppulin *et al.* functionalized the surface of GNPs with p-MBA and a pyridyldithiol-biotin compound as well as the cell surface with a sulfo-NHS-ester-biotin compound.[68] Thanks to biotin binding, the GNPs functionalized with p-MBA were localized at the cell surface and extracellular *p*H in proximity of the cell membrane was selectively measured by SERS imaging. Hosogi *et al.* replaced *p*H-sensitive p-MBA with H_2O_2-sensitive 4-mercaptophenylboronic acid pinacol ester to measure hydrogen peroxide (H_2O_2).[69] Measuring the substances associated with cell signaling at the cell surface will help understand multicellular dynamics.

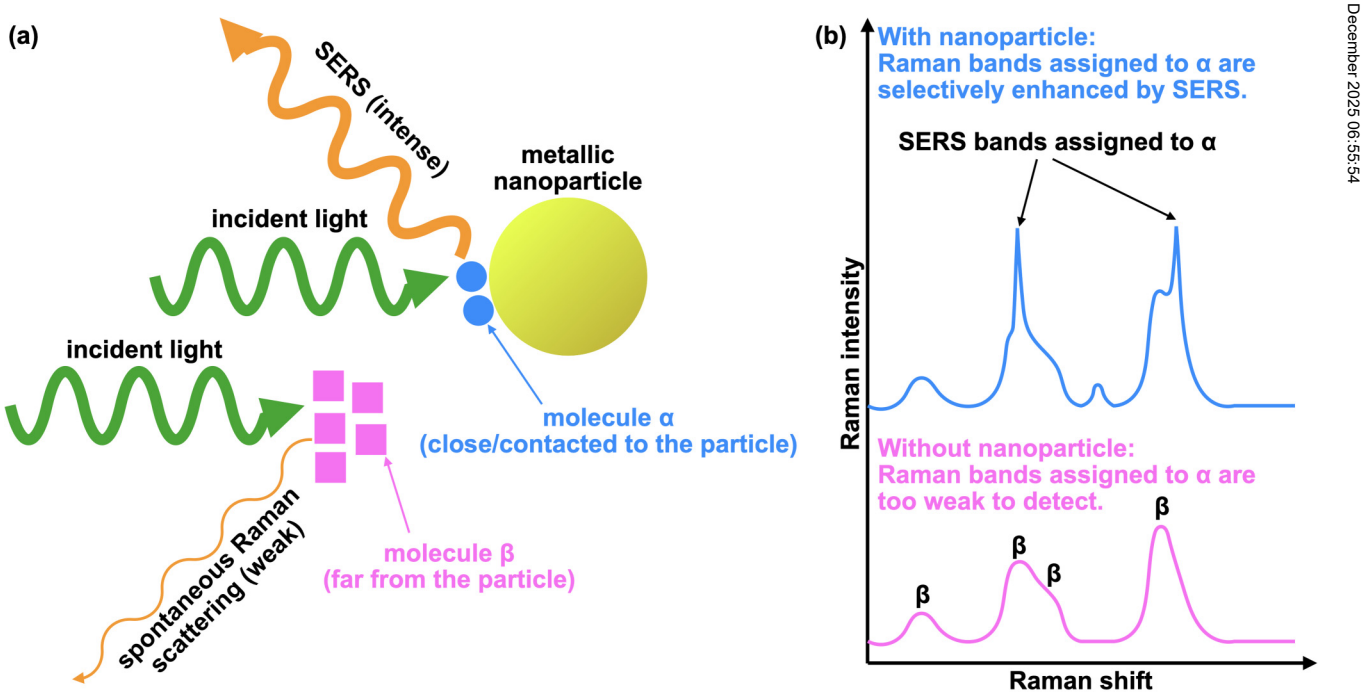

FIG. 13. Schematic illustrations of (a) the SERS effect and (b) the selective Raman enhancement by SERS. In (a), the SERS effect occurs only for the molecules near the metallic nanoparticle (molecules α). In (b), selective enhancement of the Raman signals from molecules α occurs with the metallic nanoparticle. Without the metallic nanoparticle, the Raman signals of molecules α are too weak to detect.

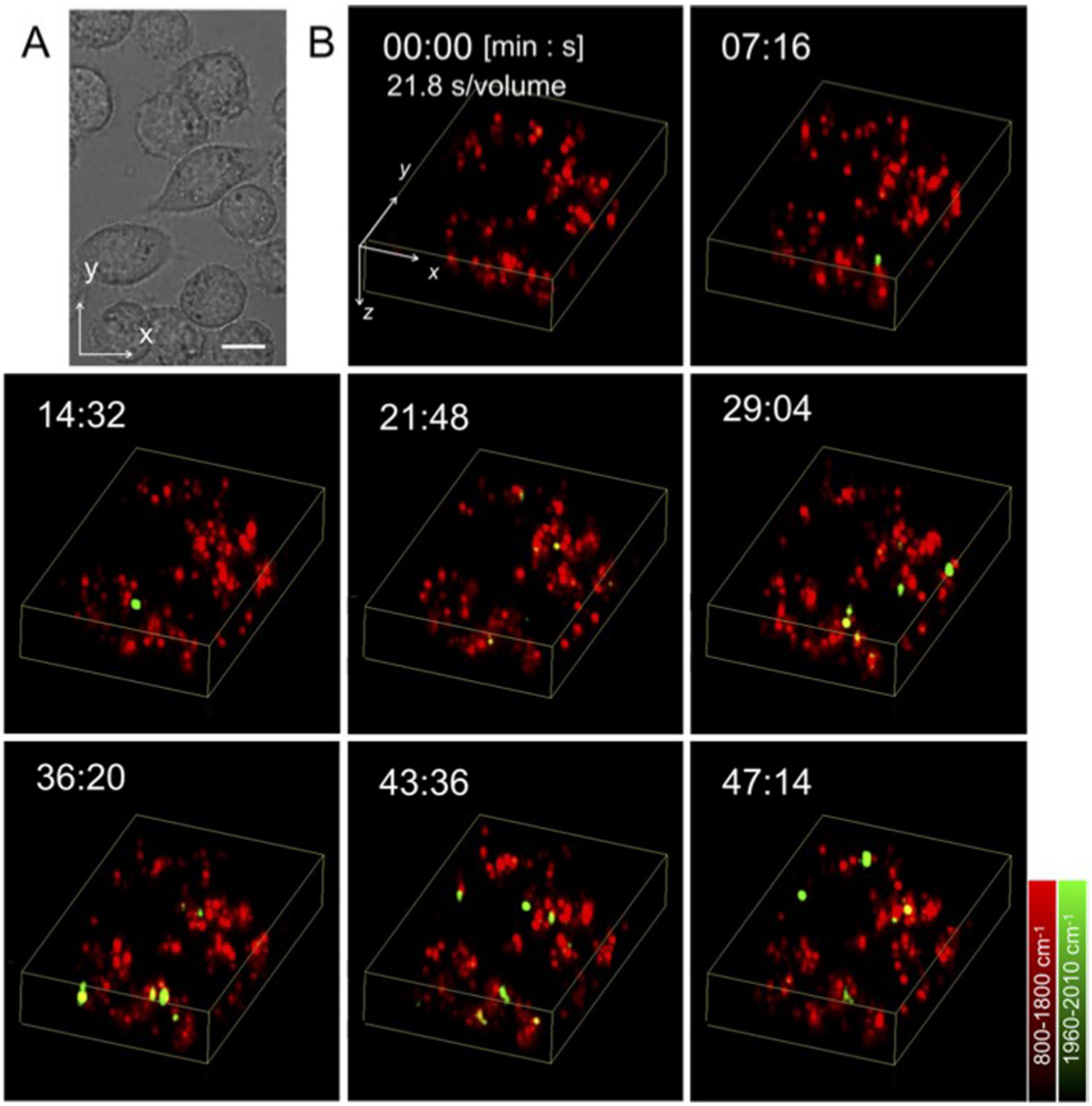

FIG. 14. Time-lapse three-dimensional SERS imaging of living macrophages. (A) Bright-field image of the cells. The scale bar shows 10 μm. (B) Representative volumes of the imaging movie. Red color represents the SERS intensity attributed to cellular endogenous molecules (i.e., average intensity at 800–1800 cm^{-1}). Green color represents the SERS intensity attributed to Alt-AOMK alkyne (i.e., average intensity at 1960–2010 cm^{-1}). The timeline indicates the time passing after drug administration into the cell culturing dish. The imaging area was 50 × 81 × 15 μm^3. Reproduced with permission from Koike *et al.*, ACS Nano B **14**, 15032 (2020). Copyright 2020 American Chemical Society.

Endogenous molecules can also be selectively enhanced using SERS. A single macrophage cell was observed under the endocytosis process by incorporating GNPs by slit-scanning Raman microscopy.[70] The SERS signals appeared after the addition of GNPs into the cell solution, and the SERS spectrum fluctuated over time. Because the intracellular compounds only in the close vicinity of the GNPs contributed to the selective enhancement of Raman scattering, the spectral fluctuation implied that the molecules near the

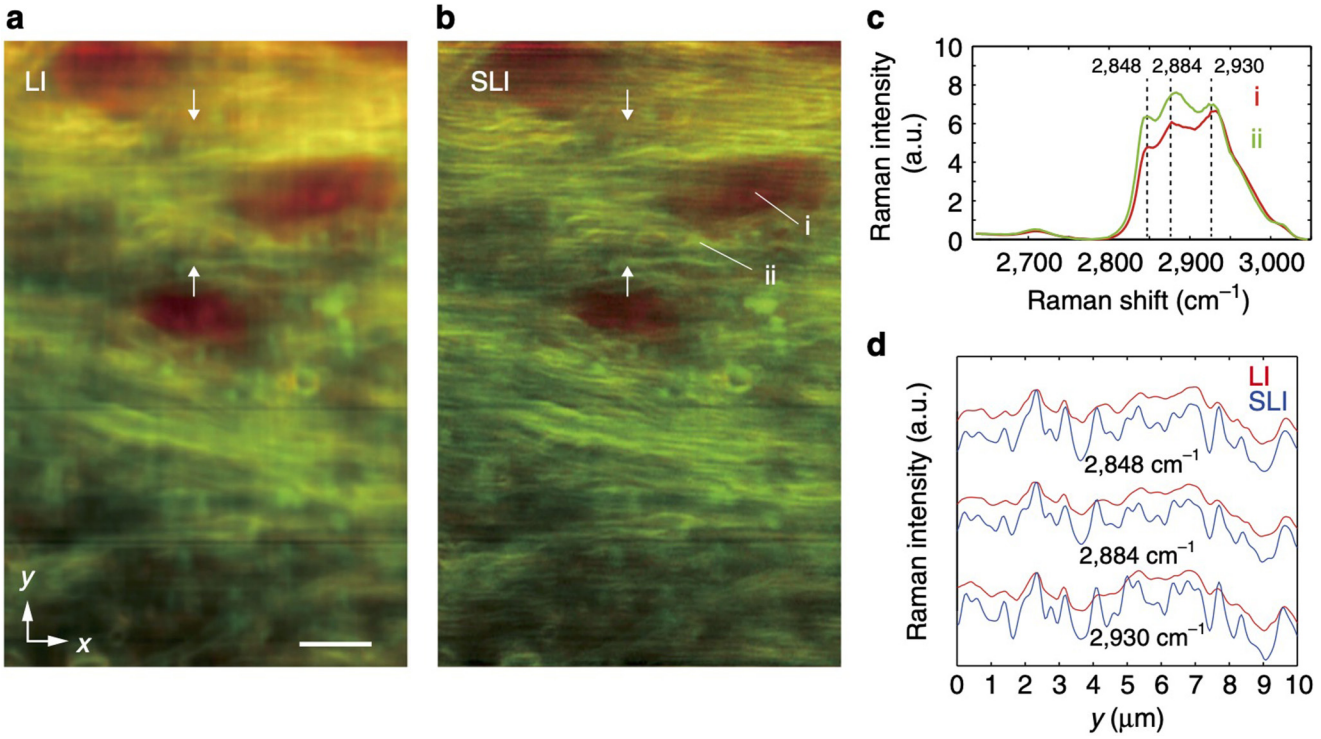

FIG. 15. Mouse brain tissue measured by (a) conventional slit-scanning Raman microscopy and (b) structured line illumination Raman microscopy. The intensity distributions of Raman peaks at 1682 cm^{-1} (amide-I) and 2848 cm^{-1} (CH_2 symmetric stretching) are shown in red and green, respectively. Scale bar represents 5 μm. (c) Representative spectra of the mouse brain sample. The spectra were taken from the positions (i) and (ii) in (b). (d) The line profiles of the slit-scanning and structured line-illumination Raman images at the positions indicated by arrows are shown for 2848, 2884, and 2930 cm^{-1}. From Watanabe *et al.*, Nat. Commun. **6**, 10095 (2015). Copyright 2015 Author(s), licensed under a Creative Commons Attribution (CC BY 4.0) license.

particles were changed during the transport of the nanoparticles by endocytosis.

Live-cell SERS imaging requires optimized experimental conditions. GNPs or gold-coated silver nanoparticles are used as SERS mediators because they are less toxic to live cells. The nanoparticle size is typically around 50 nm, as such particles can be effectively incorporated into living cells by the endocytosis process.[71] The endocytosed GNPs can finally be accumulated into lysosomes with an incubation time of 16–20h,[72] but it may also depend on cellular types. Surface modification of GNPs with a signal peptide allows organelle-selective delivery of nanoparticles.[73]

In addition to nanoparticle size, the laser wavelength for SERS excitation must be properly tailored. This is because the enhancement factor of the SERS effect as well as gold photoluminescence, which can hinder the Raman measurement, largely depends on the excitation wavelength. For GNPs with 50-nm diameter, a laser wavelength in the range of 660–785 nm is often used. With excitation at ~550 nm, where the 50-nm GNP nanoparticle has a plasmon resonance peak, the gold photoluminescence is high and hinders the SERS measurement.

Spectrophotometer detectors also need the proper selection for fast SERS imaging. In SERS imaging, the exposure time is as short as several tens of milliseconds, i.e., far shorter than that in spontaneous Raman imaging. For such a short exposure, the cooled CCD camera that is widely used for Raman imaging is not suitable because the readout rate for the cooled CCD camera is as low as mentioned above. Use of an electron-multiplying (EM) CCD camera or a scientific CMOS (sCMOS) camera with a faster readout rate (10–100 MHz) and a high quantum yield is more suitable for faster SERS imaging.

The sample irradiation also needs to be tailored properly. Spontaneous Raman imaging of living cells requires 10 $mJ/\mu m^2$ or larger to obtain a Raman spectrum with a good SNR, whereas SERS imaging requires ~25 $\mu J/\mu m^2$. If the irradiation in SERS imaging is as high as that in spontaneous Raman imaging, the cell can gain damage via the enhanced field as well as the heat generated at the GNPs.

XI. DUAL-POLARIZATION RAMAN DETECTION

In the Raman spectrum of cells or tissues, intracellular molecular bands overlap, as mentioned above. A polarization Raman detection technique can moderate the spectral overlap in the Raman spectra of cells or tissues. This is because resonance Raman

scattering can be largely depolarized and separated from non-resonance Raman scattering, which is hardly depolarized.[74]

The concept of separating resonance and non-resonance components by polarization was implemented in a slit-scanning Raman microscope.[75] A Wollaston prism was added between the edge filter and the imaging lens in front of the spectrophotometer, enabling simultaneous detection of two orthogonally polarized Raman scattering by a single spectrophotometer. Using this method, the image contrast of the resonance signals from the reduced cyt *c* as well as the non-resonance signals from phenylalanine, amide-III, and CH_2 bending was enhanced.

XII. SUPER-RESOLUTION TECHNIQUES

Advanced developments in slit-scanning Raman microscopy include super-resolution techniques. Watanabe *et al.* reported super-resolution slit-scanning Raman microscopy based on structured illumination microscopy (SIM).[16] Line illumination was structured by the interference of two line beams focused on the sample plane. Owing to the spatial distribution in a sample, structured line illumination generated the moiré pattern of a one-dimensional Raman scattering image. The moiré fringe containing the spatial information of the sample had a higher spatial frequency than the cutoff frequency of the optical system. The moiré fringes of the one-dimensional hyperspectral Raman images were recorded with three different phases, 0, $2\pi/3$, and $4\pi/3$, using a spectrophotometer equipped with a two-dimensional sensor array. After the extraction of the higher frequency components followed by a reconstruction process, a one-dimensional super-resolution hyperspectral Raman image was obtained. Using the ordinary slit-scanning process, two-dimensional hyperspectral Raman images were acquired with a resolution enhancement in the line axis direction.

Figures 15(a) and 15(b) show mouse brain tissue measured by conventional slit-scanning Raman microscopy and structured line illumination Raman microscopy, respectively. Lipids and protein beta sheets are shown in the images. The two results are apparently different; in the case of structured line illumination, the finer structures are resolved.

Structured line illumination can also aid in the identification of specific molecules in a sample. With the structured line-illumination technique, spectral overlap among different compounds can be suppressed. This is because the detection volume is reduced; hence, the number of compounds spatially overlapped in a sample spot decreases.

Super-resolution imaging techniques have been investigated for different types of coherent Raman scattering, including stimulated Raman scattering (SRS) and coherent anti-Stokes Raman scattering (CARS) microscopy, which have been summarized in other studies, such as Ref. 76.

XIII. DISCUSSION

Raman spectroscopy allows the molecular analysis of a biological sample without any labeling or invasive treatment. In combination with microscopy, it has enabled label-free biomolecular imaging and analysis of cells and tissues by hyperspectral Raman imaging. Multiplexing spatial sampling by slit-scanning Raman microscopy has improved the measurement speed of hyperspectral Raman imaging by two orders of magnitude and has expanded the applications of Raman microscopy. Advanced techniques in slit-scanning Raman microscopy have also been developed, where improvements in molecular detection specificity and spatial resolution, as well as further improvements in imaging speed, have been achieved.

Many studies have focused on improving the speed of Raman imaging. The approaches for realizing the speed improvement can be grouped into four categories, including the one we already discussed above, i.e., (1) multiplexing spatial sampling. The other three approaches include (2) enhancing Raman scattering, (3) reducing the number of total spatial sampling points, and (4) reducing noise during and after measurement. Below, we discuss these approaches and compare them with slit-scanning Raman microscopy.

Multifocus Raman microscopy is another method of multiplexing spatial sampling.[77,78] Multifocus Raman microscopy utilizes multiple beam foci arranged in a two-dimensional space, e.g., on a square grid intersection, for multiplexing spatial sampling. A hyperspectral Raman image is acquired by scanning a sample with multiple foci. Overlapping of spectra from different irradiated sites at the spectrophotometer detector is avoided by, e.g., use of a bundle of fibers that are arranged correspondingly to the beam pattern at one side and rearranged to the spectrophotometer entrance slit at the other side for detection.[77] In multifocus Raman microscopy, two-axes confocality is obtained by the fiber array or a pinhole array.

In multifocus Raman microscopy, the spectral crosstalk between foci must be considered. This is because Raman scattering from two spatially separated locations are neighbored at the spectrophotometer detector. To avoid crosstalk, multifocus Raman microscopy generally has fewer simultaneous sampling points than slit-scanning Raman microscopy.

Some applications do not require high spatial resolution in Raman imaging but just require Raman spectra sampled at multiple points within the sample. In such applications, multifocus Raman spectroscopy is more useful than the slit-scanning technique because regularly distributed two-dimensional measurement points can provide a two-dimensional distribution of Raman spectra from fixed positions in a sample. For example, the detection of intraoperative peripheral nerves using multifocus Raman spectroscopy was presented.[79] Recently, a multifocus Raman spectrometer was optimized for the measurement of samples in a multi-well format for a high-throughput biochemical analysis.[80] Variable-multipoint Raman spectroscopy was also developed and studied for intraoperative tumor margin diagnosis.[81]

Next, we discuss the Raman enhancement approach. Raman scattering can be enhanced when coherently irradiated with incident laser light. Coherent Raman scattering, including SRS and CARS, is induced by two highly intense optical pulses with different frequencies, ν_1 and ν_2. Coherent Raman processes can occur when the beat frequency $\nu_1 - \nu_2$ ($\nu_1 > \nu_2$) matches the frequency of the vibrational mode. By using ultrashort pulses to excite nonlinear Raman processes and by emitting signal photons coherently and directionally, the coherent Raman signal can reach at 10^6-fold or more of the spontaneous Raman signal. Consequently, coherent Raman scattering does not require long signal accumulation times. Coherent Raman microscopy has enabled video-rate molecular imaging of living samples, such as living mouse[82] and living cells.[83] Such high-speed imaging has not been achieved using slit-scanning

Raman microscopy. Wide applications of high-speed imaging using coherent Raman microscopy have been pursued.[9,10,11]

Sample photodamage has been an important topic in coherent Raman microscopy because the ultrashort pulses with high peak power are used to irradiate a sample.[9,11,82,84–86] The sample photodamage in coherent Raman microscopy can be explained by plasma generation through nonlinear multiphoton absorption processes, subsequently generated shockwaves, and vibrational absorption by coherent Raman processes.[84] These phenomena associated with sample photodamage largely depends on various imaging parameters such as pulse width, pulse repetition rate, optical wavelength, laser power, and the vibrational frequency. It is important to tune the experimental conditions and select an application suitable for coherent Raman imaging without causing significant sample damage.

Sample photodamage can also occur during slit-scanning Raman microscopy. Sample photodamage is remarkable when shorter visible light, i.e., violet to green light, and UV light are used.[31,87,88] Endogenous pigments can absorb light at these wavelength ranges and be directly damaged via ionization, bond cleavage, and isomerization, as well as generate reactive oxygen species and damage the sample. To avoid sample damage, we typically optimize the laser intensity, exposure time, and scanning step size depending on the application.[8,41]

A major advantage of slit-scanning Raman microscopy over coherent Raman microscopy is its simplicity of measurement. In coherent Raman microscopy, two short optical pulses must overlap in both space and time. Spectral dispersion of laser pulses in time by optical elements and a sample must be considered and compensated.[89] For hyperspectral imaging, it is necessary that one of the two pulsed lasers is either tunable or broadband, requiring another consideration for pulse shaping. In addition, the spectral resolution in coherent Raman imaging using a pulsed laser is typically poorer, and modification such as spectral focusing is necessary for high spectral resolution in coherent Raman imaging.[86] Besides, the signal photons need to be separated from the excitation pulses in SRS microscopy by lock-in detection. In comparison, slit-scanning Raman microscopy only needs to consider the damage to the sample and optical elements by high-power contunuous-wave (CW) laser irradiation. However, a major disadvantage of slit-scanning Raman microscopy is its speed, as mentioned above.

As mentioned in Sec. X, the SERS effect also enhances Raman scattering. SERS has also been used for accelerating Raman imaging.[15,67] Improvement of Raman imaging speed by SERS is limited to molecules near hotspots, and SERS imaging results depend on the hotspot distribution in a sample. Furthermore, the state of a live sample can be affected by metals.

Third, we cover the reduction of total spatial sampling points to improve the imaging speed. The simplest way to realize this approach is to use *a priori* information for selecting the sampling location over a sample.[90] Kong *et al.* used this approach to develop a method for rapid diagnosis of tumors during tissue-conserving surgery.[91] They used autofluorescence imaging to acquire *a priori* spatial information on a surgically resected skin tissue sample. The sample region was segmented by collagen and tryptophan autofluorescence intensities, and the sampling points were selected. Only 500–1500 spectral samples were sufficient for the accurate diagnosis of ~1 cm^2 tissue section samples.

A unique method using *a priori* sample information for fast Raman imaging of living cells has also been developed.[92] GNPs were used to select the sampling point. The GNPs were incorporated in living cells by endocytosis and was tracked by dark-field scattering microscopy. The particle moving inside the cell by the cellular transport function was irradiated continuously by a Raman excitation laser beam steered with a pair of galvanometer mirrors, and time-lapse SERS spectra were acquired associated with the particle transport dynamics. In this experiment, a frame rate of 20 Hz was achieved owing to the large signal generated by SERS and single-point sampling. Hence, dynamic molecular imaging of cellular transport pathways has been enabled using this unique approach. This method was expanded to three-dimensional imaging by introducing a three-dimensional particle tracking system based on dual-focus dark-field scattering microscopy as well as a z-axis sample stage.[93]

Selective spatial sampling does not always require *a priori* sampling information. Random-walk Raman microscopy, which does not require *a priori* sample information for selecting spatial sampling in confocal Raman microscopy, was recently reported.[94] This unique method first conducts random sampling. When a certain signal is detected at a given position, its surroundings are sampled. By considering the entropy of the acquired signals, the measurement can be stopped without full sampling.

When the region of interest over a sample is either sparsely distributed or localized, selective sampling can be more useful than the slit-scanning technique. However, selective sampling may miss the information that is important for the analysis. Methods have been developed to estimate the signals at unsampled locations. The compressed sensing approach introduced in Sec. VIII conducts sparse sampling and mathematically estimates unsampled data from the properties of the measurement system. In imaging applications of compressed sensing, a large positive correlation between two neighboring spatial data points is often considered. In Raman hyperspectral imaging, the correlation among spectral data points can also be considered.[95] The signal estimation for unsampled locations can also be based on statistical information. Deep-learning pre-trained models were used to estimate a high-resolution Raman image from a low-resolution one,[96] in which artifacts need to be considered.

Finally, we cover reducing noise during and after measurement. Large noise leads to longer signal accumulation in measurement to acquire data with a satisfactorily high SNR. To reduce noise, it is important to use an optical configuration that provides less noise in the measurement as well as to suppress autofluorescence from a sample. It is also possible to perform a post-measurement process to reduce the noise. The posterior processes can be categorized into two. One is the separation of noise and signal components by, e.g., singular value decomposition and Fourier transform.[8,30] The other is the signal estimation by, e.g., compressed sensing and deep learning.[97] However, the posterior process can generate artifacts in the data.

Slit-scanning Raman microscopy is further accelerated when combined with other high-speed Raman imaging approaches using, e.g., compressed sensing,[57,99] SERS,[15,67,70] machine learning,[98] and coherent Raman scattering.[100] Further multiplexing the spatial sampling can also improve the imaging speed in the slit-scanning

technique, e.g., by using a larger imager sensor or by multiple illumination lines. One of the drawbacks in the further multiplexing can be requirement of a higher laser power. A higher laser power leads to an increase in the level of background light generated from a sample substrate and optical elements and, consequently, causes a decrease in the molecular detection sensitivity of Raman measurement. To avoid such a drop in the detection sensitivity, side illumination of a sample with a 0th-order Bessel beam can be helpful because the side illumination does not generate background light in the detection path.[101]

In conclusion, slit-scanning Raman microscopy is a powerful tool for high-speed molecular imaging of cells and tissues either with or without labeling. We believe that molecular imaging by high-speed Raman microscopy will assist future discoveries in life sciences as well as the future establishment of clinical technologies.

ACKNOWLEDGMENTS

The authors thank Professor Hitoshi Hashimoto and Professor Atsushi Kasai of the Department of Pharmaceutical Sciences at Osaka University for providing the mouse brain tissue sample and helping with our interpretation of the Raman imaging results. The authors also thank Dr. Kentaro Mochizuki, currently of the Department of Pathology and Cell Regulation at Kyoto Prefectural University of Medicine, for providing the cell and tissue Raman hyperspectral imaging data. This work was partially supported by the Japan Science and Technology Agency (JST) under Grant No. JPMJCR1925 and by JST COI-NEXT under Grant No. JPMJPF2009.

AUTHOR DECLARATIONS

Conflict of Interest

The authors have no conflicts to disclose.

Author Contributions

Yasuaki Kumamoto: Conceptualization (equal); Data curation (equal); Formal analysis (equal); Investigation (equal); Methodology (equal); Software (equal); Writing – original draft (equal); Writing – review & editing (equal). **Menglu Li:** Formal analysis (equal); Investigation (equal); Methodology (equal); Writing – review & editing (equal). **Kota Koike:** Data curation (equal); Formal analysis (equal); Investigation (equal); Methodology (equal); Writing – review & editing (equal). **Katsumasa Fujita:** Conceptualization (equal); Resources (equal); Supervision (equal); Writing – review & editing (equal).

DATA AVAILABILITY

The data that support the findings of this study are available from the corresponding author upon reasonable request.

REFERENCES

[1]H. Nishimura, M. Nose, H. Hiai, N. Minato, and T. Honjo, Immunity **11**, 141–151 (1999).
[2]X. Liu, L. J. Zwiebel, D. Hinton, S. Benzer, J. C. Hall, and M. Rosbash, J. Neurosci. **12**, 2735–2744 (1992).
[3]K. Takeshige, M. Baba, S. Tsuboi, T. Noda, and Y. Ohsumi, J. Cell Biol. **119**, 301–311 (1992).
[4]K. Takahashi and S. Yamanaka, Cell **126**, 663–676 (2006).
[5]H. Cheng, W. J. Lederer, and M. B. Cannell, Science **262**, 740–744 (1993).
[6]J. W. Dani, A. Chernjavsky, and S. J. Smith, Neuron **8**, 429–440 (1992).
[7]O. Shimomura, F. H. Johnson, and Y. Saiga, J. Cellular Comparative Physiol. **59**, 223–239 (1962).
[8]A. F. Palonpon, J. Ando, H. Yamakoshi, K. Dodo, M. Sodeoka, S. Kawata, and K. Fujita, Nat. Protoc. **8**, 677–692 (2013).
[9]C. H. Camp Jr., and M. T. Cicerone, Nat. Photonics **9**, 295–305 (2015).
[10]J.-X. Cheng and X. S. Xie, Science **350**, aaa8870 (2015).
[11]C. Krafft, M. Schmitt, I. W. Schie, D. Cialla-May, C. Matthäus, T. Bocklitz, and J. Popp, Angew. Chem. Int. Ed. **56**, 4392–4430 (2017).
[12]Y. Kumamoto, Y. Harada, T. Takamatsu, and H. Tanaka, Acta Histochem. Cytochem. **51**, 101–110 (2018).
[13]K. Hamada, K. Fujita, N. I. Smith, M. Kobayashi, Y. Inouye, and S. Kawata, J. Biomed. Opt. **13**, 1 (2008).
[14]Y. Kumamoto, K. Mochizuki, K. Hashimoto, Y. Harada, H. Tanaka, and K. Fujita, J. Phys. Chem. B **123**, 2654–2661 (2019).
[15]K. Koike, K. Bando, J. Ando, H. Yamakoshi, N. Terayama, K. Dodo, N. I. Smith, M. Sodeoka, and K. Fujita, ACS Nano **14**, 15032–15041 (2020).
[16]K. Watanabe, A. F. Palonpon, N. I. Smith, L.-d. Chiu, A. Kasai, H. Hashimoto, S. Kawata, and K. Fujita, Nat. Commun. **6**, 10095 (2015).
[17]C. V. Raman and K. S. Krishnan, Nature **121**, 501–502 (1928).
[18]C. V. Raman, F. R. S., and K. S. Krishnan, Indian J. Phys. **2**, 399 (1928).
[19]J. L. Koenig, J. Polym. Sci. Macromol. Rev. **6**, 59–177 (1972).
[20]J. De Gelder, K. De Gussem, P. Vandenabeele, and L. Moens, J. Raman Spectrosc. **38**, 1133–1147 (2007).
[21]Z. Movasaghi, S. Rehman, and I. U. Rehman, Appl. Spectrosc. Rev. **42**, 493–541 (2007).
[22]A. Rygula, K. Majzner, K. M. Marzec, A. Kaczor, M. Pilarczyk, and M. Baranska, J. Raman Spectrosc. **44**, 1061–1076 (2013).
[23]K. Czamara, K. Majzner, M. Z. Pacia, K. Kochan, A. Kaczor, and M. Baranska, J. Raman Spectrosc. **46**, 4–20 (2015).
[24]B. R. Wood and D. McNaughton, J. Raman Spectrosc. **33**, 517–523 (2002).
[25]A. Dorosz, M. Grosicki, J. Dylas, E. Matuszyk, M. Rodewald, T. Meyer, J. Popp, K. Malek, and M. Baranska, Cells **9**, 2041 (2020).
[26]N. A. Brazhe, M. Treiman, A. R. Brazhe, N. L. Find, G. V. Maksimov, and O. V. Sosnovtseva, PLoS ONE **7**, e41990 (2012).
[27]S. Stewart, D. A. Shea, C. P. Tarnowski, M. D. Morris, D. Wang, R. Franceschi, D.-L. Lin, and E. Keller, J. Raman Spectrosc. **33**, 536–543 (2002).
[28]A. Shen, Z. Liao, H. Wang, I. Goan, Y. Wu, X. Wang, Z. Yu, and J. Hu, J. Biomed. Opt. **12**, 034003 (2007).
[29]T. Minamikawa, Y. Harada, and T. Takamatsu, Sci. Rep. **5**, 17165 (2015).
[30]A. Mahadevan-Jansen and R. Richards-Kortum, J. Biomed. Opt. **1**, 31 (1996).
[31]Y. Kumamoto, A. Taguchi, and S. Kawata, Adv. Opt. Mater. **7**, 1801099 (2019).
[32]S. Chadha, W. H. Nelson, and J. F. Sperry, Rev. Sci. Instrum. **64**, 3088–3093 (1993).
[33]S. Kawata, T. Ichimura, A. Taguchi, and Y. Kumamoto, Chem. Rev. **117**, 4983–5001 (2017).
[34]R. P. Van Duyne, D. L. Jeanmaire, and D. F. Shriver, Anal. Chem. **46**, 213–222 (1974).
[35]J. M. Friedman and R. M. Hochstrasser, Chem. Phys. Lett. **33**, 225–227 (1975).
[36]J. Funfschilling and D. F. Williams, Appl. Spectrosc. **30**, 443–446 (1976).
[37]S. M. Angel, M. K. DeArmond, K. W. Hanck, and D. W. Wertz, Anal. Chem. **56**, 3000–3001 (1984).
[38]G. Penel, G. Leroy, and E. Bres, Appl. Spectrosc. **52**, 312–313 (1998).
[39]D. A. Shea and M. D. Morris, Appl. Spectrosc. **56**, 182–186 (2002).
[40]G. J. Puppels, F. F. M. de Mul, C. Otto, J. Greve, M. Robert-Nicoud, D. J. Arndt-Jovin, and T. M. Jovin, Nature **347**, 301–303 (1990).
[41]M. Okada, N. I. Smith, A. F. Palonpon, H. Endo, S. Kawata, M. Sodeoka, and K. Fujita, Proc. Natl. Acad. Sci. U.S.A. **109**, 28–32 (2012).

[42]A. T. Lewis, R. Gaifulina, M. Isabelle, J. Dorney, M. L. Woods, G. R. Lloyd, K. Lau, M. Rodriguez-Justo, C. Kendall, N. Stone, and G. M. Thomas, J. Raman Spectrosc. **48**, 119–125 (2017).
[43]J. Qi and W.-C. Shih, Appl. Opt. **53**, 2881 (2014).
[44]I. W. Schie, L. Alber, A. L. Gryshuk, and J. W. Chan, Analyst **139**, 2726–2733 (2014).
[45]Y. Harada, P. Dai, Y. Yamaoka, M. Ogawa, H. Tanaka, K. Nosaka, K. Akaji, and T. Takamatsu, Histochem. Cell Biol. **132**, 39–46 (2009).
[46]A. Hashimoto, Y. Yamaguchi, L.-d. Chiu, C. Morimoto, K. Fujita, M. Takadachi, S. Kawata, S. Murakami, and E. Tamiya, Sci. Rep. **5**, 12529 (2015).
[47]J. N. Taylor, K. Mochizuki, K. Hashimoto, Y. Kumamoto, Y. Harada, K. Fujita, and T. Komatsuzaki, J. Phys. Chem. B **123**, 4358–4372 (2019).
[48]M. Ogawa, Y. Harada, Y. Yamaoka, K. Fujita, H. Yaku, and T. Takamatsu, Biochem. Biophys. Res. Commun. **382**, 370–374 (2009).
[49]N. Nishiki-Muranishi, Y. Harada, T. Minamikawa, Y. Yamaoka, P. Dai, H. Yaku, and T. Takamatsu, Anal. Chem. **86**, 6903–6910 (2014).
[50]T. Yamamoto, T. Minamikawa, Y. Harada, Y. Yamaoka, H. Tanaka, H. Yaku, and T. Takamatsu, Sci. Rep. **8**, 14671 (2018).
[51]T. Minamikawa, Y. Harada, N. Koizumi, K. Okihara, K. Kamoi, A. Yanagisawa, and T. Takamatsu, Histochem. Cell Biol. **139**, 181–193 (2013).
[52]Y. Zhou, C.-H. Liu, B. Wu, X. Yu, G. Cheng, K. Zhu, K. Wang, C. Zhang, M. Zhao, R. Zong, L. Zhang, L. Shi, and R. R. Alfano, J. Biomed. Opt. **24**, 095001 (2019).
[53]B. Lochocki, B. D. C. Boon, S. R. Verheul, L. Zada, J. J. M. Hoozemans, F. Ariese, and J. F. de Boer, Commun. Biol. **4**, 474 (2021).
[54]N. M. Honarvar, A. Saedisomeolia, M. Abdolahi, A. Shayeganrad, G. T. Sangsari, B. H. Rad, and G. Muench, J. Mol. Neurosci. **61**, 289–304 (2017).
[55]I. W. Schie, C. Krafft, and J. Popp, J. Biophotonics **9**, 994–1000 (2016).
[56]S. Duraipandian, W. Zheng, J. Ng, J. J. H. Low, A. Ilancheran, and Z. Huang, Analyst **136**, 4328 (2011).
[57]N. Pavillon and N. I. Smith, Opt. Express **24**, 30038 (2016).
[58]Y. Oshima, H. Sato, H. Kajiura-Kobayashi, T. Kimura, K. Naruse, and S. Nonaka, Opt. Express **20**, 16195 (2012).
[59]H. Yamakoshi, K. Dodo, M. Okada, J. Ando, A. Palonpon, K. Fujita, S. Kawata, and M. Sodeoka, J. Am. Chem. Soc. **133**, 6102–6105 (2011).
[60]H. Yamakoshi, K. Dodo, A. Palonpon, J. Ando, K. Fujita, S. Kawata, and M. Sodeoka, J. Am. Chem. Soc. **134**, 20681–20689 (2012).
[61]F. Hu, C. Zeng, R. Long, Y. Miao, L. Wei, Q. Xu, and W. Min, Nat. Methods **15**, 194–200 (2018).
[62]S. Egoshi, K. Dodo, K. Ohgane, and M. Sodeoka, Org. Biomol. Chem. **19**, 8232–8236 (2021).
[63]H. Yamakoshi, A. Palonpon, K. Dodo, J. Ando, S. Kawata, K. Fujita, and M. Sodeoka, Bioorg. Med. Chem. Lett. **25**, 664–667 (2015).
[64]S. Bakthavatsalam, K. Dodo, and M. Sodeoka, RSC Chem. Biol. **2**, 1415–1429 (2021).
[65]H. Yamakoshi, A. F. Palonpon, K. Dodo, J. Ando, S. Kawata, K. Fujita, and M. Sodeoka, Chem. Commun. **50**, 1341–1343 (2014).
[66]L. Shi, C. Zheng, Y. Shen, Z. Chen, E. S. Silveira, L. Zhang, M. Wei, C. Liu, C. de Sena-Tomas, K. Targoff, and W. Min, Nat. Commun. **9**, 2995 (2018).
[67]Z. Zhang, K. Bando, K. Mochizuki, A. Taguchi, K. Fujita, and S. Kawata, Anal. Chem. **91**, 3254–3262 (2019).
[68]L. Puppulin, S. Hosogi, H. Sun, K. Matsuo, T. Inui, Y. Kumamoto, T. Suzaki, H. Tanaka, and Y. Marunaka, Nat. Commun. **9**, 5278 (2018).
[69]S. Hosogi, Y. Marunaka, E. Ashihara, T. Yamada, A. Sumino, H. Tanaka, and L. Puppulin, Biosens. Bioelectron. **179**, 113077 (2021).
[70]K. Fujita, S. Ishitobi, K. Hamada, N. I. Smith, A. Taguchi, Y. Inouye, and S. Kawata, J. Biomed. Opt. **14**, 024038 (2009).
[71]J. Kneipp, H. Kneipp, M. McLaughlin, D. Brown, and K. Kneipp, Nano Lett. **6**, 2225–2231 (2006).
[72]M. Liu, Q. Li, L. Liang, J. Li, K. Wang, J. Li, M. Lv, N. Chen, H. Sing, J. Lee, J. Shi, L. Wang, R. Lal, and C. Fan, Nat. Commun. **8**, 15646 (2017).
[73]A. Huefner, W.-L. Kuan, R. A. Barker, and S. Mahajan, Nano Lett. **13**, 2463–2470 (2013).
[74]T. G. Spiro and T. C. Strekas, Proc. Natl. Acad. Sci. U.S.A. **69**, 2622–2626 (1972).
[75]L.-d. Chiu, A. F. Palonpon, N. I. Smith, S. Kawata, M. Sodeoka, and K. Fujita, J. Biophotonics **8**, 546–554 (2015).
[76]K. Fujita, "Super-resolution imaging in Raman microscopy," in *Label-Free Super-Resolution Microscopy*, edited by V. Astratov (Springer Nature Switzerland. AG, 2019), Vol. 8, p. 195.
[77]M. Okuno and H. Hamaguchi, Opt. Lett. **35**, 4096 (2010).
[78]S. Yabumoto and H. Hamaguchi, Anal. Chem. **89**, 7291–7296 (2017).
[79]Y. Kumamoto, Y. Harada, H. Tanaka, and T. Takamatsu, Sci. Rep. **7**, 845 (2017).
[80]H. Kawagoe, J. Ando, M. Asanuma, K. Dodo, T. Miyano, H. Ueda, M. Sodeoka, and K. Fujita, Sci. Rep. **11**, 15742 (2021).
[81]F. Sinjab, K. Kong, G. Gibson, S. Varma, H. Williams, M. Padgett, and I. Notingher, Biomed. Opt. Express **7**, 2993 (2016).
[82]C. L. Evans, E. O. Potma, M. Puoris'haag, D. Côté, C. P. Lin, and X. S. Xie, Proc. Natl. Acad. Sci. U.S.A. **102**, 16807–16812 (2005).
[83]B. G. Saar, C. W. Freudiger, J. Reichman, C. M. Stanley, G. R. Holtom, and X. S. Xie, Science **330**, 1368–1370 (2010).
[84]Y. Fu, H. Wang, R. Shi, and J.-X. Cheng, Opt. Express **14**, 3942 (2006).
[85]D. Zhang, M. N. Slipchenko, and J.-X. Cheng, J. Phys. Chem. Lett. **2**, 1248–1253 (2011).
[86]K. Koike, N. I. Smith, and K. Fujita, Biomed. Opt. Express **13**, 995 (2022).
[87]G. J. Puppels, J. H. F. Olminkhof, G. M. J. Segers-Nolten, C. Otto, F. F. M. De Mul, and J. Greve, Exp. Cell Res. **195**, 361–367 (1991).
[88]Y. Kumamoto, A. Taguchi, N. I. Smith, and S. Kawata, Biomed. Opt. Express **2**, 927 (2011).
[89]M. Lindley, J. G. de Pablo, R. Kinegawa, K. Hiramatsu, and K. Goda, Opt. Lett. **46**, 4320 (2021).
[90]J. Qi, J. Li, and W.-C. Shih, Biomed. Opt. Express **4**, 2376 (2013).
[91]K. Kong, C. J. Rowlands, S. Varma, W. Perkins, I. H. Leach, A. A. Koloydenko, H. C. Williams, and I. Notingher, Proc. Natl. Acad. Sci. U.S.A. **110**, 15189–15194 (2013).
[92]J. Ando, K. Fujita, N. I. Smith, and S. Kawata, Nano Lett. **11**, 5344–5348 (2011).
[93]K.-C. Huang, K. Bando, J. Ando, N. I. Smith, K. Fujita, and S. Kawata, Methods **68**, 348–353 (2014).
[94]S. Kawata, Proc. SPIE **11098**, 1109803 (2019).
[95]F. Soldevila, J. Dong, E. Tajahuerce, S. Gigan, and H. B. de Aguiar, Optica **6**, 341 (2019).
[96]C. C. Horgan, M. Jansen, A. Nagelkerke, J.-P. St-Pierre, T. Vercauteren, M. M. Stevens, and M. S. Bergholt, Anal. Chem. **93**, 15850–15860 (2021).
[97]N. Yamato, H. Niioka, J. Miyake, and M. Hashimoto, Sci. Rep. **10**, 15212 (2020).
[98]H. He, M. Xu, C. Zong, P. Zheng, L. Luo, L. Wang, and B. Ren, Anal. Chem. **91**, 7070–7077 (2019).
[99]C. Scotté, S. Sivankutty, R. A. Bartels, and H. Rigneault, Opt. Lett. **45**, 5567 (2020).
[100]S. Kizawa and M. Hashimoto, J. Chem. Phys. **155**, 144201 (2021).
[101]K. Bando, S. Yabuuchi, M. Li, T. Kubo, R. Oketani, N. I. Smith, and K. Fujita, Biomed. Opt. Express **13**, 3161 (2022).